Mapping Urban Heat Vulnerability in London: Multi-Scale Geospatial Analysis Using Machine Learning, SHAP Explainability, and Temporal Mortality Data

Adesuyi Adeoti[a,*] William Alston[a]

[a] *School of Physics, Engineering, and Computer Science; Department of Physics, Astronomy, and Mathematics; University of Hertfordshire, Hatfield, United Kingdom*

* Corresponding author. E-mail address: aa24aie@herts.ac.uk (A. Adeoti)

Data and code availability

The analysis pipeline is archived on Zenodo (https://doi.org/10.5281/zenodo.21785934), and an interactive dashboard is available at london-heat-vulnerability.streamlit.app. See the Data Availability statement within the manuscript for full details.

How to cite

Adeoti, A., & Alston, W. (2026). Mapping Urban Heat Vulnerability in London: Multi-Scale Geospatial Analysis Using Machine Learning, SHAP Explainability, and Temporal Mortality Data [Preprint]. EarthArXiv.

Mapping Urban Heat Vulnerability in London: Multi-Scale Geospatial Analysis Using Machine Learning, SHAP Explainability, and Temporal Mortality Data

Adesuyi Adeoti[a,*], William Alston[a]

[a] *School of Physics, Engineering, and Computer Science; Department of Physics, Astronomy, and Mathematics; University of Hertfordshire, Hatfield, United Kingdom*

*Corresponding author. E-mail address: aa24aie@herts.ac.uk (A. Adeoti)

Abstract

Urban heat is a significant cause of mortality. In London, during the summer of 2022, the United Kingdom experienced its first recorded 40°C day, resulting in excess mortality levels not observed since pre-antibiotic influenza seasons. On 19 July 2022, London reached a temperature of 40.3°C, the highest recorded in the United Kingdom, which corresponded to 18,435 excess deaths in England and Wales. This study develops the first Lower Layer Super Output Area (LSOA)-scale heat vulnerability index (VI) for all 33 London Boroughs ($n = 4{,}994$) by integrating eight distinct datasets using a reproducible six-script Python pipeline. A critical methodological step involved identifying and excluding seven variables that leaked data, thereby reducing the maximum feature-VI correlation from 1.000 to 0.772. Five machine learning models were trained and validated spatially using borough-based data splitting. The four best-performing models achieved Test R^2 scores between 0.864 and 0.873, with overlapping 95% bootstrap confidence intervals, indicating that model learnability is not dependent on specific architectural choices. XGBoost is the main model (Test $R^2 = 0.869$, MAE $= 0.161$); the SHAP attribution shows HVI_mean (|SHAP| mean = 0.272) and imd_employment_score (0.216) as co-dominant drivers in all five architectures. Temporal trend analysis from 2015 to 2024 identified a pronounced asymmetry: the number of deaths increased substantially during the summer period ($\tau = 0.644$, $p = 0.012$, with 1,544 additional deaths annually), whereas temperature trends were not statistically significant ($p = 0.371$). However, seasonal-trend decomposition using LOESS (STL) indicated an underlying warming trend ($p = 0.032$). The environmental justice analysis demonstrated a vulnerability ratio of 1.30 between the most and least deprived decile groups, with 60.3% of the vulnerability index attributable to physical thermal exposure. UKCP18 projections indicate that Barnet, currently ranked 32nd among 33 boroughs, is projected to become the primary location for emerging hot spots.

Keywords: urban heat island; heat vulnerability index; machine learning; SHAP; London; environmental justice; climate projections

1. Introduction

Urban Heat Islands (UHIs) are prominent characteristics of contemporary cities, primarily resulting from the conversion of vegetated land to impervious surfaces. Oke [1] demonstrated that this land cover change alters the surface energy budget, increasing latent and sensible heat storage and causing urban temperatures to surpass those of rural areas. Peng et al. [2] reported that the mean surface urban heat island intensity across 419 major cities was 1.5°C, with the most pronounced UHIs observed in densely built temperate cities such as London. Stewart and Oke [3] developed the Local Climate Zone classification system, and subsequent research has synthesized urban overheating mitigation strategies and their associated trade-offs [28]. Intensifying heatwaves driven by climate change subject urban populations to compounded heat stress, as already elevated urban temperatures rise further during extreme weather events [4, 5].

The 2022 UK heatwave highlighted the severity of heat-related hazards. On 19 July 2022, Heathrow Airport recorded a peak temperature of 40.3°C in the United Kingdom [6]. During the summer of 2022, excess deaths in England and Wales totalled 18,435, representing a 16.6% increase compared to the five-year pre-pandemic baseline. Temporal analysis indicates that summer mortality in England and Wales has not returned to baseline levels since 2022. Consequently, a critical question for planners and health practitioners is which communities are currently most vulnerable and which are likely to become vulnerable as temperatures continue to rise.

Three significant gaps in the literature on London motivate this investigation. First, the spatial resolution in previous studies remains too coarse. The foundational study by Wolf and McGregor [7] utilized wards based on 2001 Census data, while Roberts, Sun, and Pelling [8] advanced to the output-area level but limited their analysis to a single borough, Hackney. To date, no London-wide analysis at the Lower Layer Super Output Area (LSOA) scale has been conducted. Second, there is a lack of benchmarking for machine learning models across multiple frameworks using SHAP attribution within the London context. Third, prior analyses have not separated temperature and mortality temporal trends, which, as demonstrated by the results, differ substantially from a policy perspective. This study addresses all three gaps concurrently.

The following six research questions guide the analysis of the study: (RQ1) How does thermal exposure differ for the 4,994 LSOAs in London? (RQ2) What are the SHAP values for thermal, demographic, and socioeconomic variables for five different models? (RQ3) Which is the best generalizing model using spatially blocked boroughs for model validation? (RQ4) What are the temporal patterns from 2015 to 2024, and how are they different? (RQ5) Is there a structural change in mortality due to the 2022 heat wave? (RQ6) Is there heat vulnerability burdening disadvantaged areas?

2. Theoretical Framework and Related Work

The Vulnerability Framework [4] developed by the IPCC combines hazard, sensitivity, and adaptive capacity into one definition. It was used by Reid et al. [9] to assess vulnerability to heat in U.S. census tracts, and it became evident that complex risk is found in inner-city areas. The social vulnerability framework [10] in which heat vulnerability studies are placed is clearly defined by Cutter, Boruff and Shirley.

For London, Wolf and McGregor [7] built a heat vulnerability index based on nine proxy variables derived from the 2001 census via principal component analysis (ward-level). Roberts, Sun, and Pelling [8] developed such an index for the Hackney boroughs via PCA at the output-area level and modeled air temperatures for 2022. Neither of the studies uses machine learning techniques with SHAP attribution, nor does the pan-London LSOA assessment.

The machine learning approach is based on work by Grinsztajn, Oyallon, and Varoquaux [11], which evaluates tree ensemble models and neural network performance on structured tabular datasets of similar size (approximately 10,000 samples) as used in the present study. SHAP [12] splits up prediction explanations from the model into additive feature effects using cooperative game theory. The analysis of the temporal trends uses Mann–Kendall τ [13, 14] and Sen's slope [15] tests, the most common nonparametric trend approaches. The heat mortality association is defined by Gasparrini et al. [16] and Kovats and Hajat [17]. The environmental justice approach is based on Mitchell and Chakraborty [18] and Hoffman et al. [19].

3. Data and Methodology

3.1 Study Area

Greater London is divided into 33 administrative boroughs that span a total area of 1,572 km^2 (51.5°N, 0.1°W) and show a Census 2021 population of 8.8 million. The climate of Greater London is temperate maritime (Köppen climate class Cfb), resulting in average maximum temperatures of about 23°C for the June–August period under normal conditions. The Index of Multiple Deprivation rankings (IMD 2019) identify Newham, Tower Hamlets, and Barking and Dagenham as some of the most deprived authorities in England, while Richmond upon Thames, Kingston upon Thames, and Bromley are some of the least deprived. The basic spatial unit used is the Lower Layer Super Output Area (LSOA), which represents the smallest geography for which Census 2021 and IMD 2019 data are available (about 1,000–3,000 inhabitants per LSOA). All 4,994 Greater London LSOAs are included in the study.

3.2 Data Sources

This study employs eight main datasets (Table 1). At the core of the research is a 19-scene composition of Landsat 8 Collection 2 Level-2 that offers 30 m resolution data on thermal infrared and surface reflectance for the June–August (JJA) period of 2015 to 2024, created using Google Earth Engine. The calibrated surface temperatures from Landsat 8 Collection 2 Level-2 are directly provided and do not require any further atmospheric correction. Data on building heights were collected from the Environment Agency LiDAR Composite DSM [20]; Green space coverages were calculated based on 31,685 OpenStreetMap (OSM) features; demographic data were obtained from Census 2021 (ONS Nomis); deprivation scores were retrieved from IMD 2019 (MHCLG); data on mortality rates were taken from ONS weekly death registrations; temperature data were gathered from the Met Office MIDAS Heathrow station.

Table 1. Primary datasets: source, spatial unit, and temporal coverage

Dataset	Source	Spatial unit	Coverage
Landsat 8 Collection 2 Level-2	USGS/NASA via Google Earth Engine	30 m raster	JJA 2015–2024 (19 scenes)
LiDAR Composite DSM/DTM	Environment Agency [20]	1 m → LSOA	2021–2022
OpenStreetMap green space	OSM (landuse + natural)	Polygon → LSOA	2024 extract
Census 2021 (TS007A, TS006, TS054)	ONS Nomis	LSOA 2021	2021
Index of Multiple Deprivation 2019	MHCLG	LSOA 2011	2019
ONS weekly death registrations	Office for National Statistics	National/Boroughs	2015–2024
Heathrow MIDAS station	Met Office	Point station	2015–2024
LSOA 2021 boundaries	ONS Open Geography Portal	LSOA polygon	2021

3.3 Google Earth Engine Remote Sensing Pipeline

Cloud masking was performed using the QA_PIXEL and QA_RADSAT band quality flags from Landsat 8 Collection 2 Level 2 data products, which excluded clouds, cloud shadows, and saturated pixels. A median composite was generated from 19 cloud-free June–July–August (JJA) scenes. Land Surface Temperature (LST) was derived from the ST_B10 surface temperature band. UHI intensity was measured in relation to the rural reference temperature of 31.09°C, corresponding to the median value of LST in rural pixels of Greater London. Spectral indices:

$$\mathrm{NDVI} = \frac{\mathrm{B5} - \mathrm{B4}}{\mathrm{B5} + \mathrm{B4}}$$ [21];

$$\mathrm{NDBI} = \frac{\mathrm{B6} - \mathrm{B5}}{\mathrm{B6} + \mathrm{B5}}$$ [22];

$$\mathrm{MNDWI} = \frac{\mathrm{B3} - \mathrm{B6}}{\mathrm{B3} + \mathrm{B6}}$$ [23].

The physical HVI composite is

$$\mathrm{HVI} = 0.50 \cdot \mathrm{LST} + 0.30 \cdot (1 - \mathrm{NDVI}) + 0.20 \cdot \mathrm{NDBI} \tag{1}$$

Composite rasters were aggregated to Lower Layer Super Output Area (LSOA) centroids through the application of zonal statistics, specifically mean, maximum, and standard deviation.

3.4 Vulnerability Index Construction

The Integrated Vulnerability Index (VI) applies the Intergovernmental Panel on Climate Change (IPCC) Exposure–Sensitivity–Adaptive Capacity (E–S–AC) tripartite framework [4], with equal weighting assigned to each component.

$$\mathrm{VI} = \frac{1}{3}\mathrm{E} + \frac{1}{3}\mathrm{S} + \frac{1}{3}\mathrm{AC} \tag{2}$$

Exposure (E) is defined as the normalized mean of land surface temperature (LST) and urban heat intensity (UHI). Sensitivity (S) consists of the normalized number of elderly individuals (pop_65plus, Census 2021), population density, and the IMD 2019 health deprivation factor. Adaptation Capacity (AC) comprises the normalized proportion of greenery, the inverse of the IMD 2019 income deprivation factor, and the inverse of the proportion of social rented accommodation. Each of the six sub-components was independently normalized to the range [1, 10] using the min-max method before calculating an equally weighted sum. Borough VI represents the population-weighted average of the LSOA values.

3.5 Structural Data Leakage Detection and Fixing

A key methodological advancement is the explicit identification and removal of seven structural data leakage features. Min-max normalization constitutes an affine ($x = ax + b$) transformation; any raw variable used as input to a normalized VI sub-component is algebraically equivalent to the normalized value, which allows linear models to reconstruct VI precisely. Before correction for structural leakage, the Lasso produced $R^2 = 1.000$ on both the training and the test set, an artifact of the algebraic equivalence. Seven features were dropped from further analysis: LST_mean, UHI_mean, pop_density_per_km², imd_health_score, green_space_pct, imd_income_score, and imd_living_env_score. Following the correction, the maximum absolute Pearson correlation between any feature and VI decreased from 1.000 to 0.772 (HVI_mean). This reduction suggests the existence of a valid regression problem.

3.6 Machine Learning Pipeline

Following the removal of data leakage, eleven predictors were retained: LST_max, LST_std, UHI_max, NDVI_mean, NDBI_mean, MNDWI_mean, HVI_mean, pop_65plus, imd_employment_score, mean_building_height_m, and lsoa_area_km². Spatial validation used boroughs-grouped GroupShuffleSplit (random_state = 42): 2,835 LSOAs (56.8%) for training, 1,072 (21.5%) for validation, and 1,087 (21.8%) for testing. Five different models were trained using grid search cross-validation for hyperparameter tuning: Lasso, MLP, SVM with RBF kernel, Random Forest [30], and XGBoost [29]. The model was chosen based on the following composite scoring strategy:

$$\mathrm{CS} = R^2_{\mathrm{test}} - 1.5 \times \Delta\mathrm{CV} \tag{3}$$

Where ΔCV is the generalization gap of the CV test. Performance uncertainty was quantified using bootstrap resampling to generate 95% confidence intervals based on 1,000 resamples. For SHAP attribution, TreeExplainer was used for XGBoost and Random Forest, LinearExplainer for Lasso, and KernelExplainer for SVM and MLP. Moran's I test was conducted to measure the spatial autocorrelation of the residuals.

3.7 Temporal and Environmental Justice Analysis

Three parallel time series (annual, n = 10, 2015–2024) were analyzed: average Heathrow JJA Tmax obtained via the Met Office MIDAS database, satellite-derived LST, and England and Wales summer mortality (ONS weeks 23–35). For each time series, the Mann-Kendall τ nonparametric test [13, 14] and Sen's slope [15] were computed, along with OLS regression analysis. Seasonal-Trend Decomposition using Loess (STL) [24] procedure was carried out on the Heathrow 120-month data series for separating the trend and seasonality components. Boroughs' 2022 excess mortality was calculated as the difference between the number of observed summer deaths in 2022 and the borough's baseline (2015-2019). In the environmental justice study, the association between the 2019 Income Deprivation Decile of the Index of Multiple Deprivation (IMD) and the mean Vulnerability Index (VI) in LSOA was estimated via the Spearman correlation coefficient, and the disparity ratio was calculated as a ratio of mean VI in Decile 10 to mean VI in Decile 1.

4. Results

4.1 Outputs from Remote Sensing and the Integrated Vulnerability Index

Composite images of 19 scenes of Landsat 8 JJA yielded the mean land surface temperature (LST) of 34.19°C in Greater London with the maximal pixel value of 53.18°C (Fig. 1a). Analysis at the borough level indicates an inverse east–west thermal gradient (Fig. 1b). Boroughs of inner-east London (Newham, Tower Hamlets, and Hackney) record the highest LST in London, while outer south-west boroughs are much cooler. Normalized Difference Vegetation Index (NDVI) is inversely related to land surface temperature (Fig. 2a), with Tower Hamlets and Southwark revealing mean NDVI values from 0.147 to 0.242 (Fig. 2b); Richmond and Bromley reach mean NDVI values of 0.529 to 0.624. In the area of analysis, 31.9% of LSOAs include no OpenStreetMap (OSM) green space. The mean Urban Heat Island (UHI) intensity is 3.10°C; there are 102.7 km² of extreme zones of UHI with 8°C or more (Fig. 3b); the raster of UHI for the whole city is provided in Fig. 3a. Extremely high HVI (HVI > 0.70) areas cover 267.1 km², as shown in Figure 4b; the resulting composite raster for the HVI is shown in Fig. 4a.

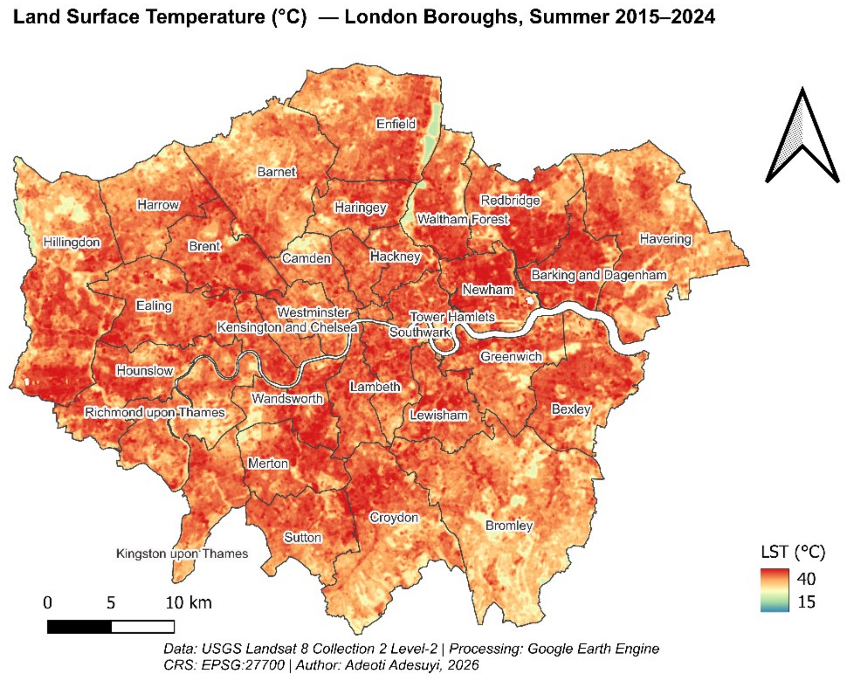

(a) 30 m LSOA-scale raster: average surface temperature of 34.19°C, maximum of 53.18°C

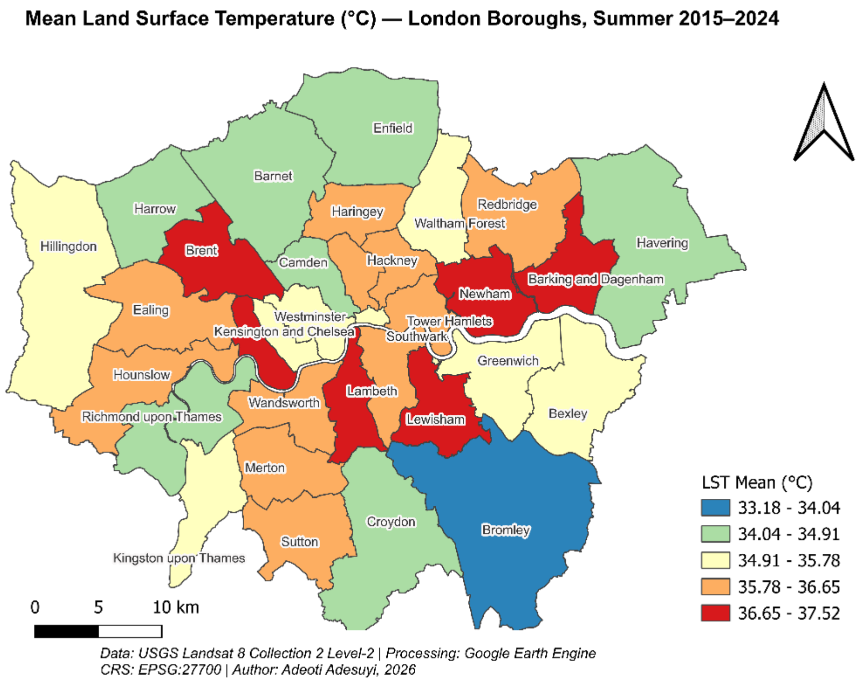

(b) Borough-level map showing thermal gradient from west to east.

Fig. 1. Land Surface Temperature over Greater London.

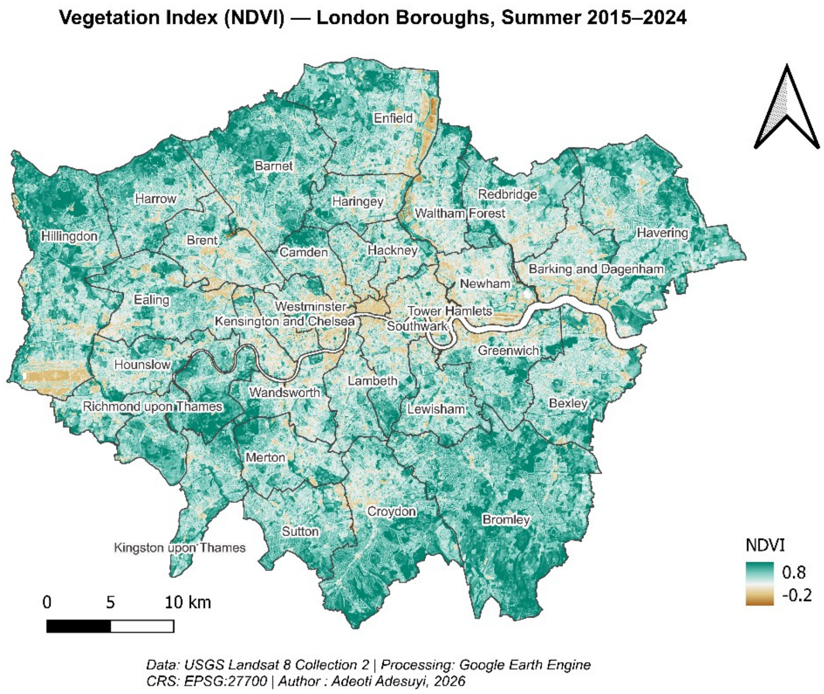

(a) 30 m NDVI raster.

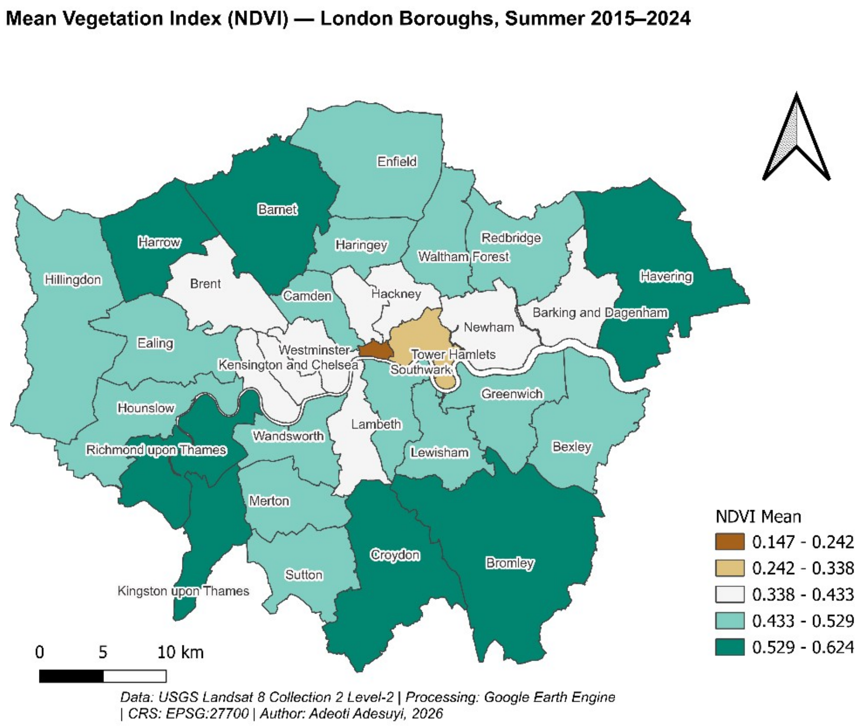

(b) Borough aggregation: Tower Hamlets and Southwark lowest; Richmond and Bromley highest.

Fig. 2. NDVI in Greater London.

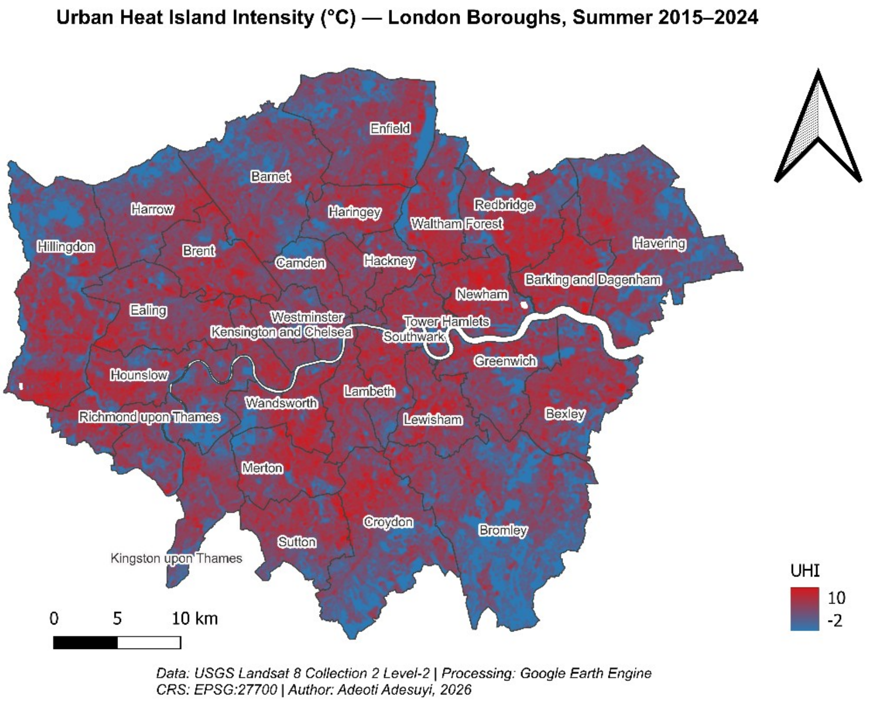

(a) City-wide UHI raster: mean 3.10°C.

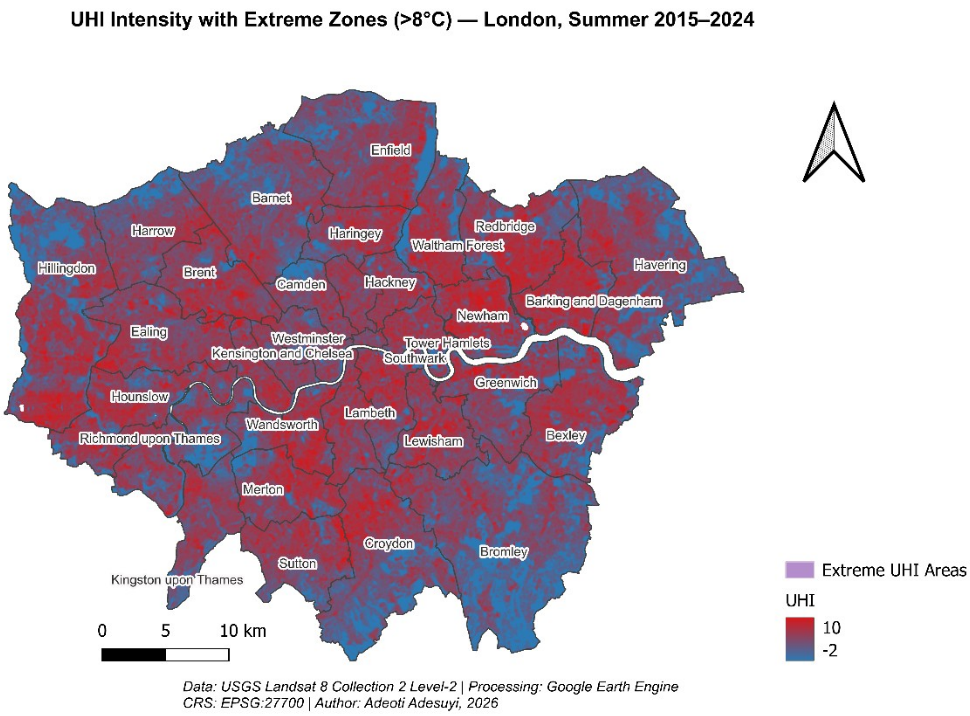

(b) Extremely strong UHI (Urban Heat Island) (above 8°C higher than rural background, 102.7 km²).

Fig. 3. Intensity of the urban heat island.

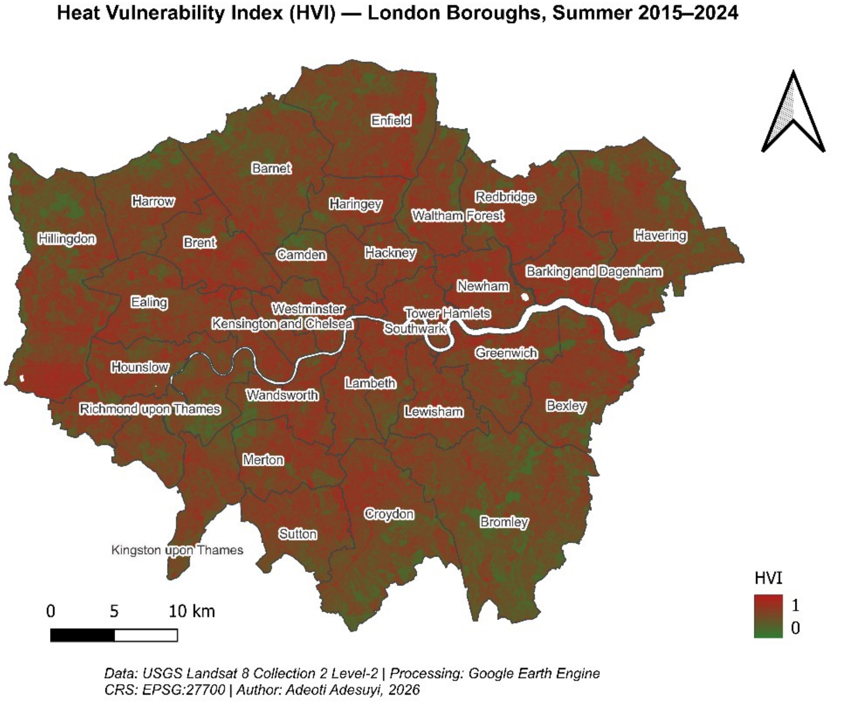

(a) Composite HVI raster.

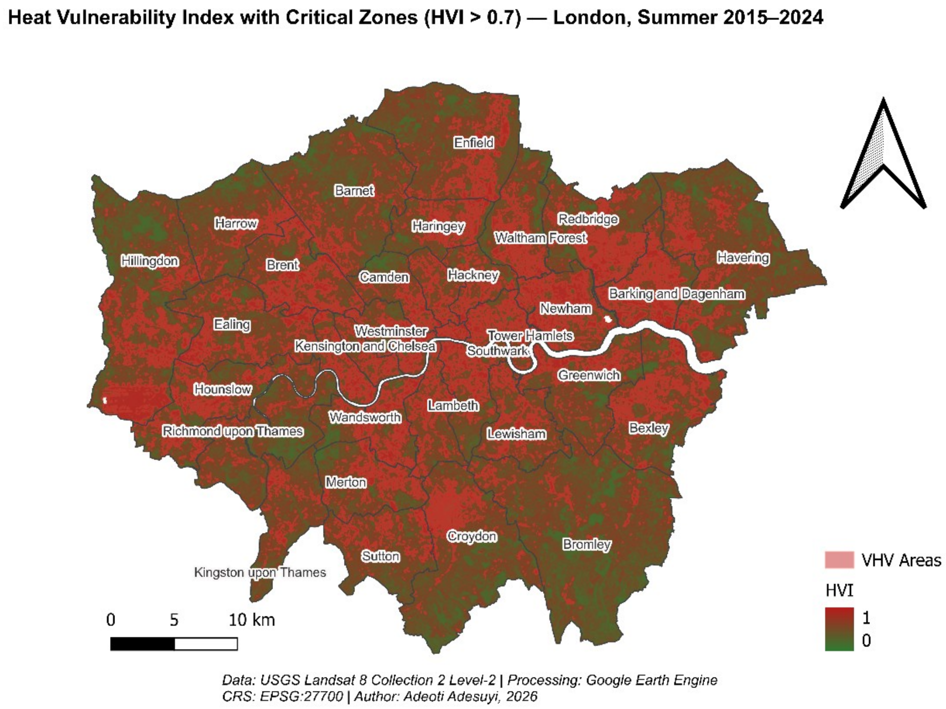

(b) Critical areas (HVI > 0.70, 267.1 km²)

Fig. 4. Physical HVI

The VI ranges between 1.88 and 6.76 (mean = 5.06, SD = 0.63) for 4,994 LSOAs, with 57.5% falling within the high vulnerability category (refer to Figure 5). Croydon 010E is identified as the most vulnerable LSOA (VI = 6.76); Croydon 015D (VI = 6.73) and Hackney 019A (VI = 6.67) follow behind. Table 2 below shows the top ten vulnerable boroughs, and Barking and Dagenham is the most vulnerable (VI = 5.59). Although Westminster has the second-highest LST class, it only stands at 23rd position because of high adaptive capacity outweighing heat exposure, and this is known as the Westminster Paradox, demonstrating the conceptual superiority of the compound tripartite index over thermal proxies alone.

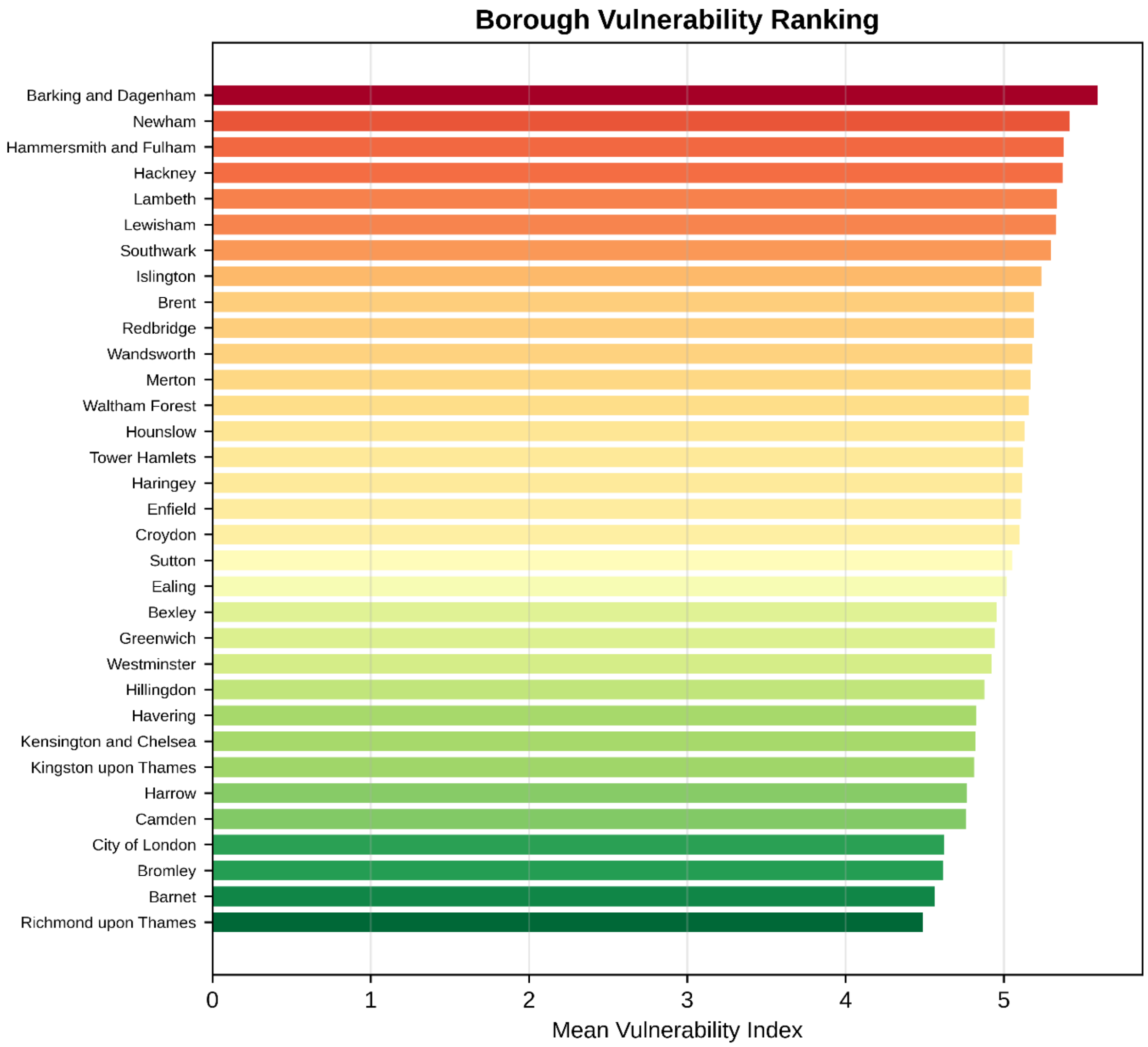

Fig. 5. Vulnerability Score Rankings for all 33 London boroughs. The borough with the highest mean vulnerability index (VI) score is Barking and Dagenham with a value of 5.59, whereas Westminster is placed 23rd even though it has the second highest LST classification, demonstrating what is known as the Westminster paradox.

Table 2. Ten London boroughs with the highest mean Vulnerability Index values

Rank	Boroughs	Mean VI	Typology
1	Barking and Dagenham	5.59	Compound Risk
2	Newham	5.42	Compound Risk
3	Hackney	5.37	Compound Risk
4	Hammersmith and Fulham	5.38	Compound Risk
5	Lambeth	5.34	Compound Risk
6	Tower Hamlets	5.33	Population Sensitivity
7	Southwark	5.30	Thermal Exposure
8	Lewisham	5.24	Compound Risk
9	Islington	5.19	Population Sensitivity
10	Greenwich	5.12	Low Adaptive Capacity

4.2 Feature Correlations and Leakage Validation

Pearson correlation coefficients between all 11 variables and the Vulnerability Index (VI) were calculated (n = 4,994) and are presented in Table 3. The highest absolute value is 0.772 (HVI_mean). Perfect collinearity (r = +1.000) exists between LST_max and UHI_max; this stems from the spatially fixed rural background temperature, implying that at the LSOA scale, LST_max and UHI_max differ only by arithmetic identity.

Table 3. Correlations between features and the target variable for the 11 selected predictors (n = 4,994 LSOAs)

Feature	r with VI	Category
HVI_mean	0.772	Physical – thermal-spectral composite
imd_employment_score	0.536	Socioeconomic – adaptive capacity
pop_65plus	−0.311	Demographic – sensitivity
NDVI_mean	−0.624	Physical – vegetation cooling
LST_max	0.598	Physical – thermal peak
UHI_max	0.598	Physical – thermal (= LST_max at LSOA)
NDBI_mean	0.542	Physical – built density
LST_std	0.489	Physical – thermal variability
MNDWI_mean	−0.371	Physical – water cooling
mean_building_height_m	0.312	Structural
lsoa_area_km²	−0.287	Spatial scale

4.3 Machine Learning Performance

The top four architectures demonstrate overlapping Test R^2 values ranging from 0.864 to 0.873, with corresponding 95% bootstrap confidence intervals also overlapping (Table 4, Figs. 6a and 6b). Predicted versus observed plots for all five architectures are presented in Fig. 6a, while train and validation generalization diagnostics are shown in Fig. 6b. The convergence observed across the five architectures suggests that the results are not attributable to model selection bias; the vulnerability signal is consistently learned from the provided features [11]. XGBoost is selected as the primary model due to its use of exact TreeSHAP attribution (Test R^2 = 0.869, MAE = 0.161, CS = 0.706), with no additional performance benefit observed among alternatives. The Lasso model achieves the highest composite score (CS = 0.840), attributed to its minimal generalization gap (0.022) and linearity. Moran's I for the XGBoost residuals is 0.312 ($z = 16.77$, $p < 0.001$).

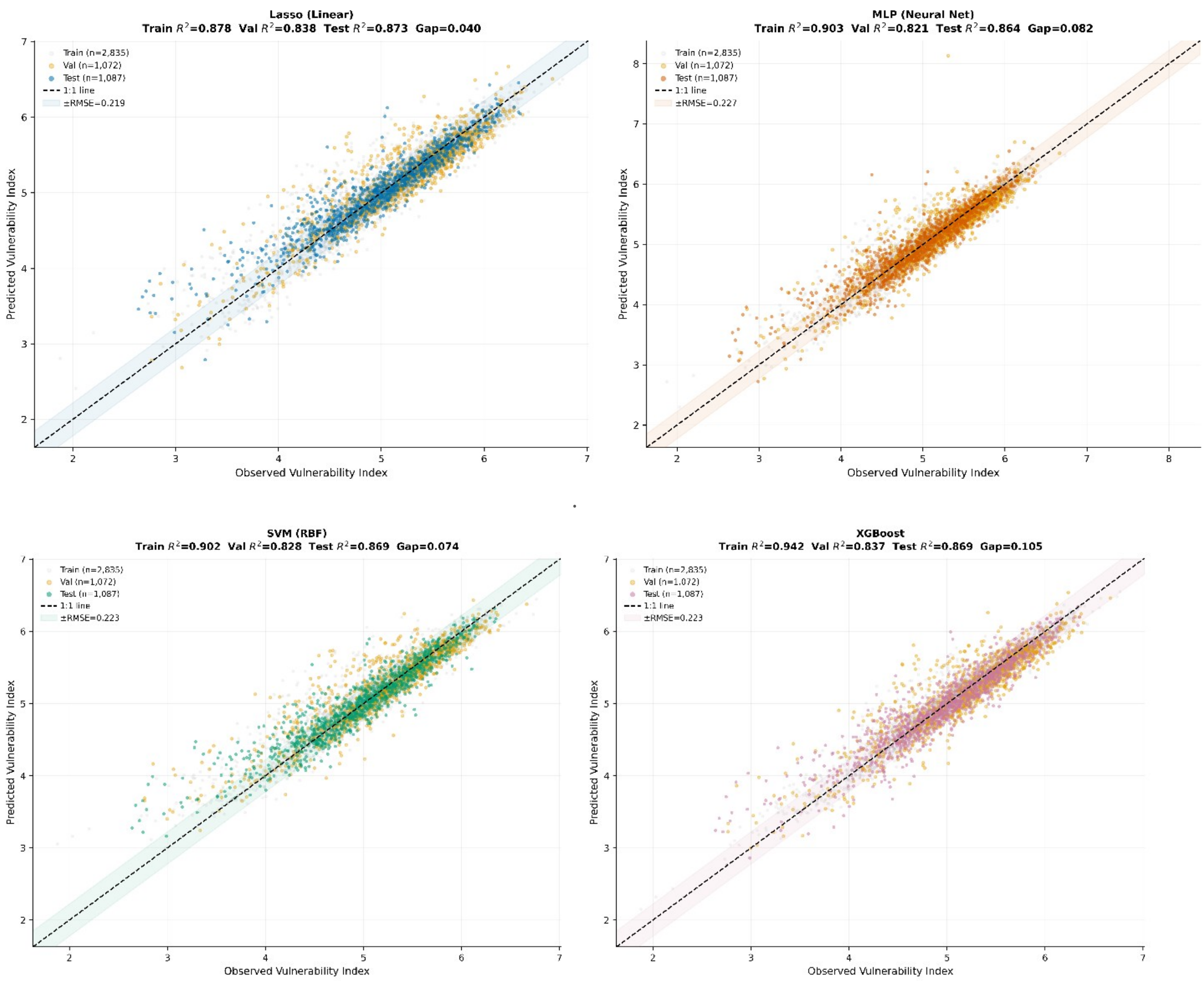

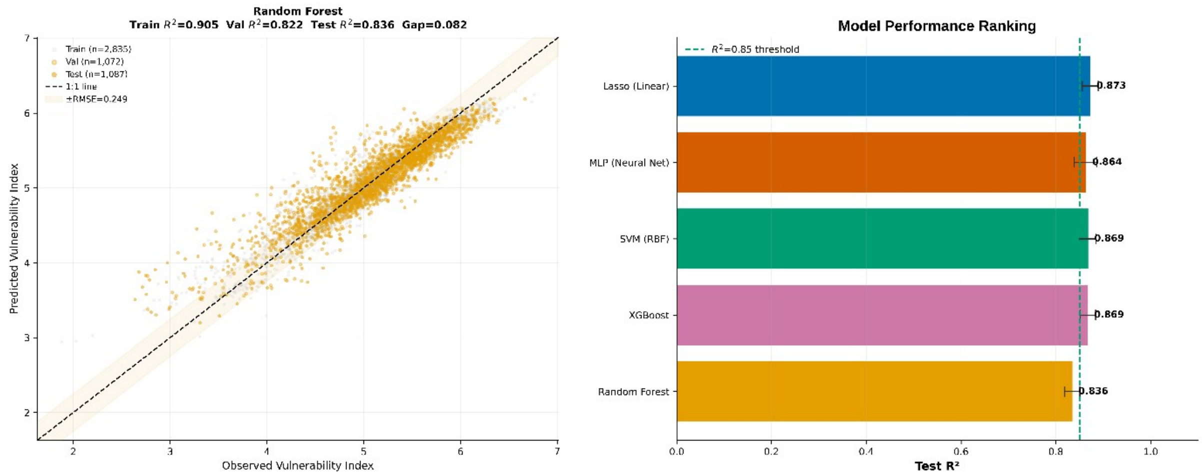

(a) Predicted vs observed VI for all five models (Test n = 1,087).

(b) Comparison of Training and Validation R² for Generalization Assessment

Fig. 6. Model performance across different architectures

Table 4. Comparison of model performance across five architectures using boroughs-blocked spatial validation.

Model	Test R²	95% CI	CV R² (mean±SD)	MAE	Spearman ρ	CS
XGBoost	0.869	[0.852, 0.883]	0.833±0.041	0.161	0.938	0.706
Lasso	0.873	[0.856, 0.889]	0.855±0.032	0.148	0.948	0.840
MLP	0.864	[0.839, 0.886]	0.838±0.043	0.159	0.940	0.766
SVM (RBF)	0.869	[0.850, 0.884]	0.825±0.065	0.152	0.944	0.754
Random Forest	0.836	[0.819, 0.851]	0.771±0.089	0.180	0.925	0.635

4.4 SHAP Feature Attribution

The average absolute SHAP values of the five architectures are provided in Table 5. Two variables stand out as dominant across all five architectures: HVI_mean is the top-ranking variable in four of the five models (XGBoost mean|SHAP|= 0.272), and imd_employment_score is the second variable in all five models (XGBoost 0.216). This two-variable dominance holds across all five model families regardless of the particular algorithm used. Based on the mean |SHAP| bar graph (Fig. 7a), it is clear that HVI_mean and imd_employment_score operate as co-dominant predictors. The XGBoost beeswarm plot (Fig. 7b) depicts the expected effects of the variables: HVI_mean positively influences the predicted VI, while NDVI_mean negatively does so; green space has a cooling effect [25, 26], and a high imd_employment_score increases VI due to the reduced ability of the people working in insecure or outdoor environments to protect themselves from heat. The cross-model SHAP consistency is illustrated in Fig. 7c.

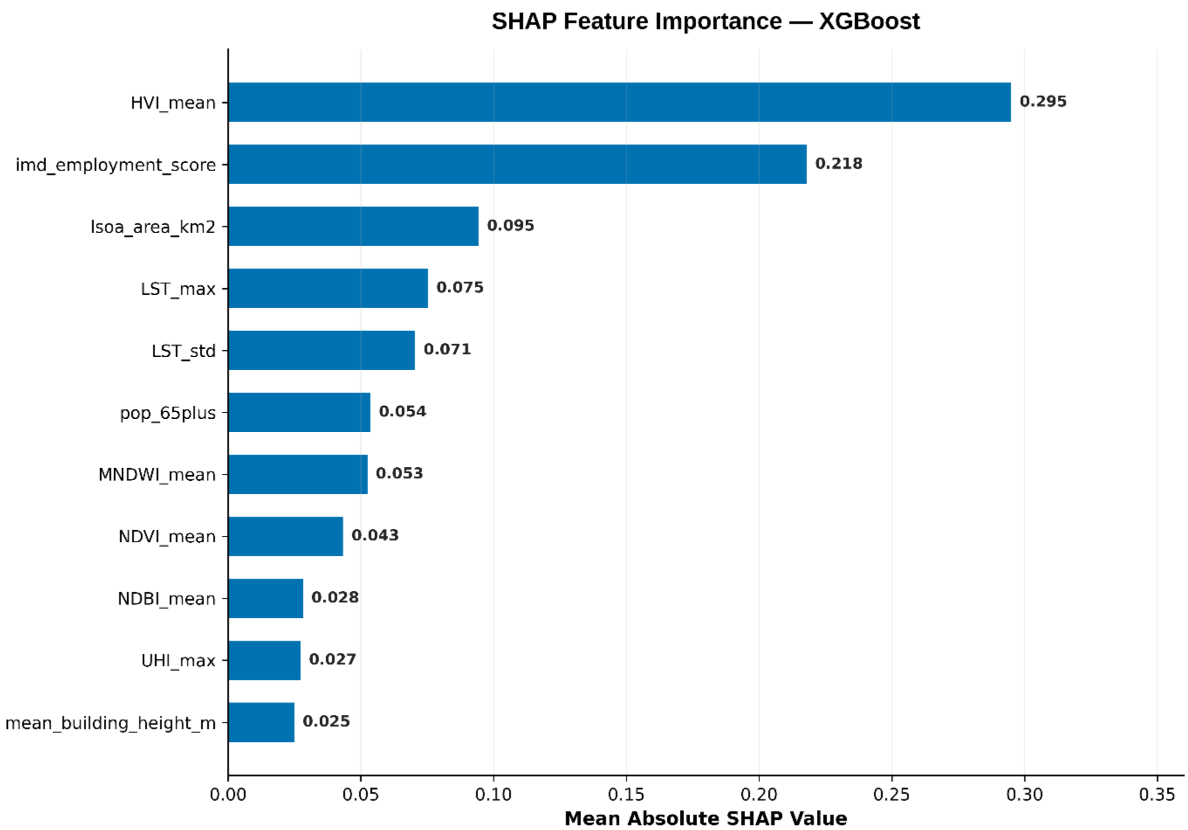

(a) Mean |SHAP| bar chart: HVI_mean and imd_employment_score co-dominant.

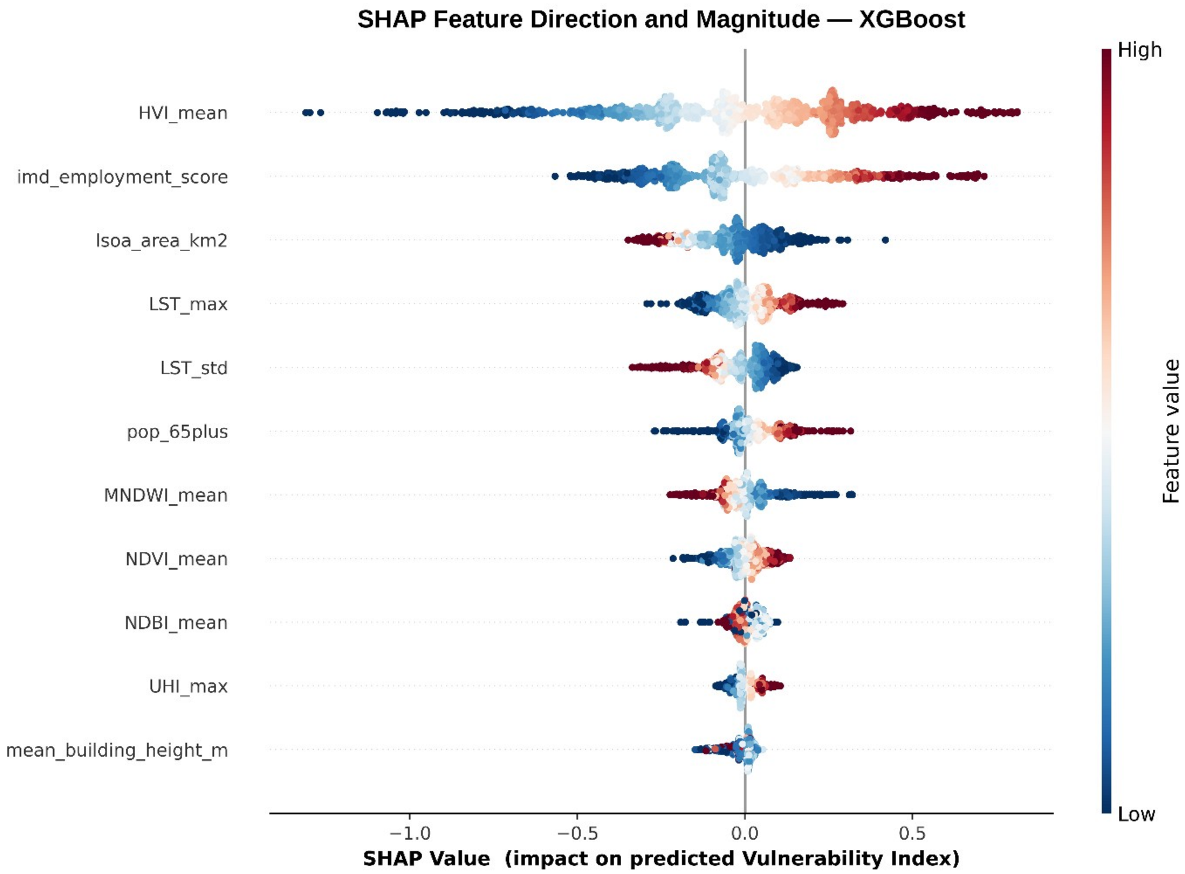

(b) XGBoost beeswarm: directional effects.

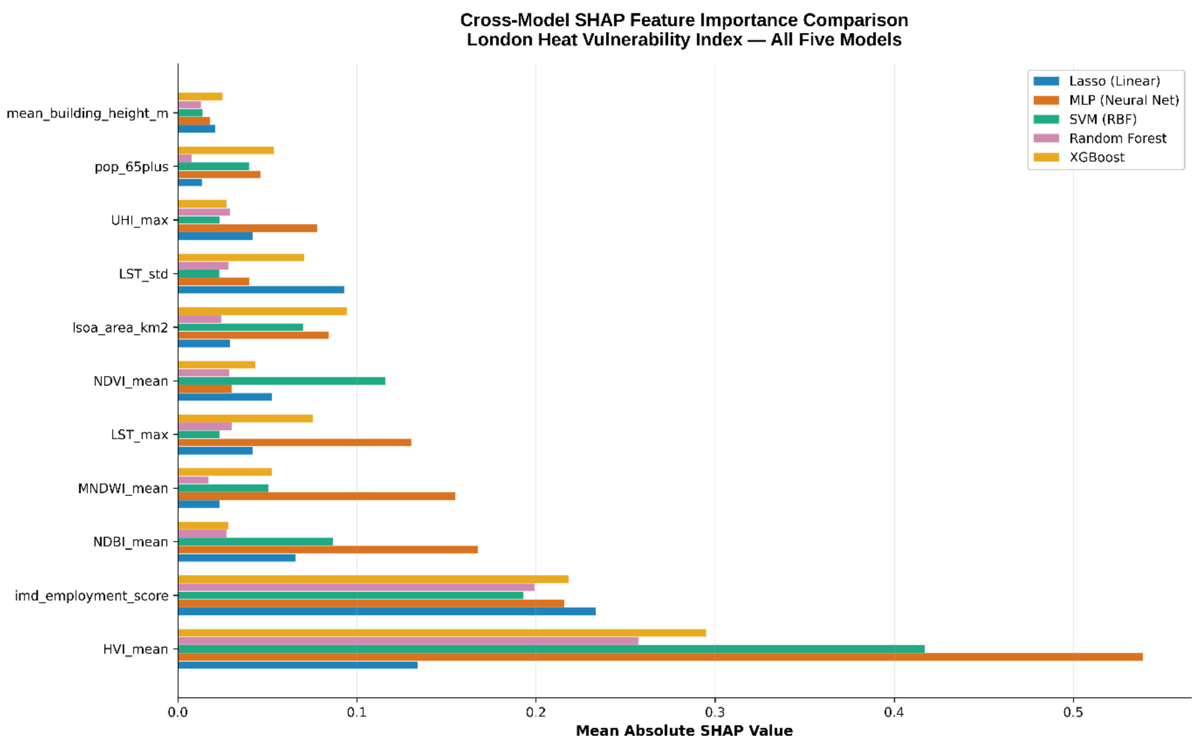

(c) Cross-model SHAP comparison.

Fig. 7. SHAP feature attribution

Table 5. Mean absolute SHAP values — top 7 features per model, ranked by XGBoost

Feature	XGBoost	Lasso	MLP	SVM	Consistent rank
HVI_mean	0.272	0.130	0.539	0.417	1st in 4/5
imd_employment_score	0.216	0.232	0.216	0.193	2nd in all
pop_65plus	0.118	0.143	0.127	0.119	3rd (majority)
NDVI_mean	0.093	0.107	0.089	0.094	4th (majority)
lsoa_area_km²	0.093	0.052	0.067	0.071	5th (XGBoost/MLP)
LST_max	0.079	0.088	0.065	0.082	6th
UHI_max	0.072	0.081	0.071	0.076	7th

4.5 Boroughs Typology

SHAP Decomposition and VI Component Analysis allocate the entire 33 boroughs into five typology clusters (Table 6). The driver profiles of the entire 33 boroughs are shown in Fig. 8a, with the distribution of typologies illustrated in Fig. 8b. Six of the boroughs show compound risks, which are characterized by peaks on all three dimensions of the IPCC. Twelve of the boroughs are shown as having low adaptive capacity, seven of them as being dominated by thermal exposure, three of them as being dominated by population sensitivity, and five of them as low-risk boroughs. Westminster is one of the low-risk boroughs; despite being in the second LST class, it is a further instance of the Westminster Paradox: adaptive capacity moderates thermal hazard where deprivation is absent.

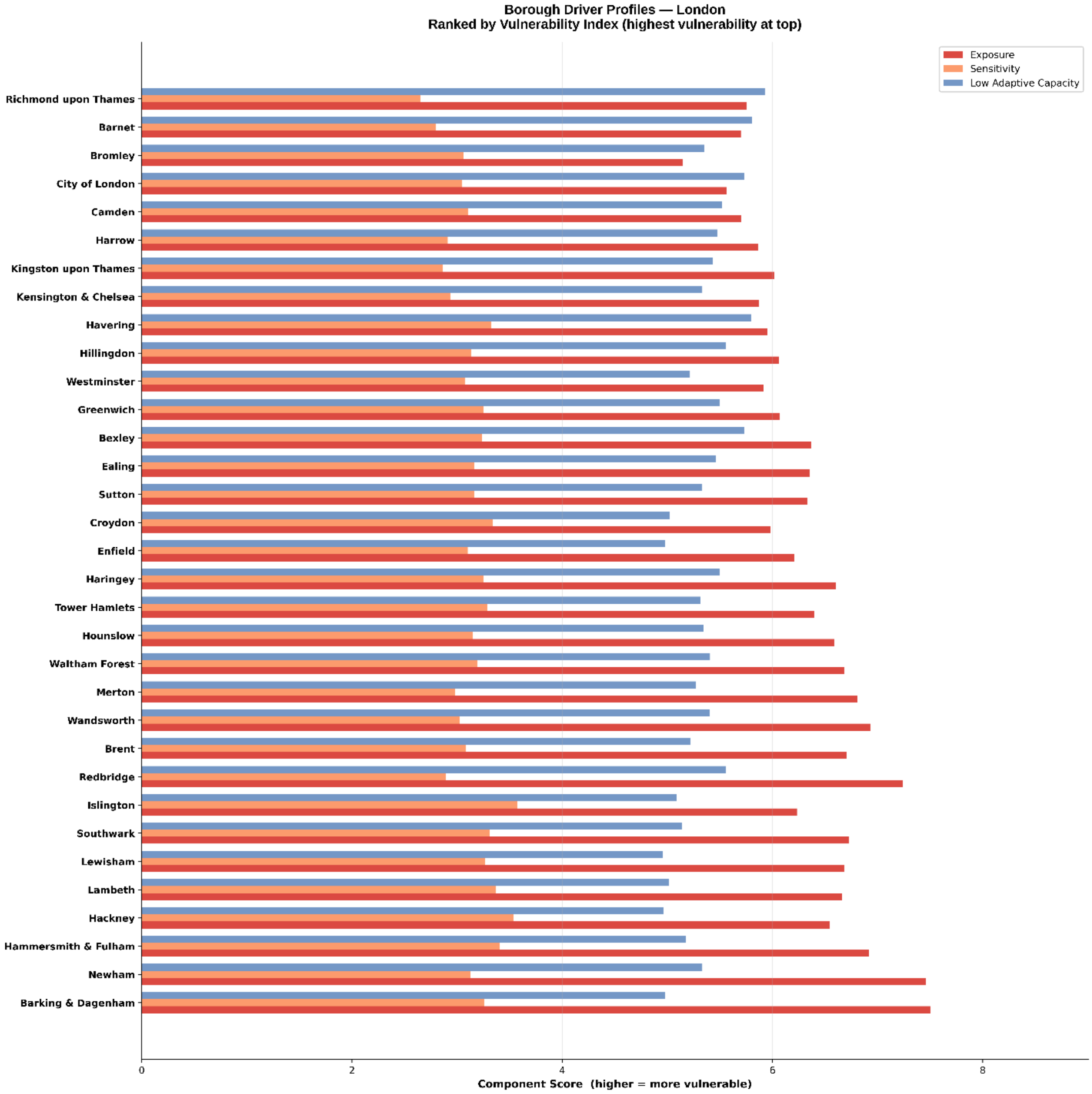

(a) Driver profile bar chart for all 33 boroughs.

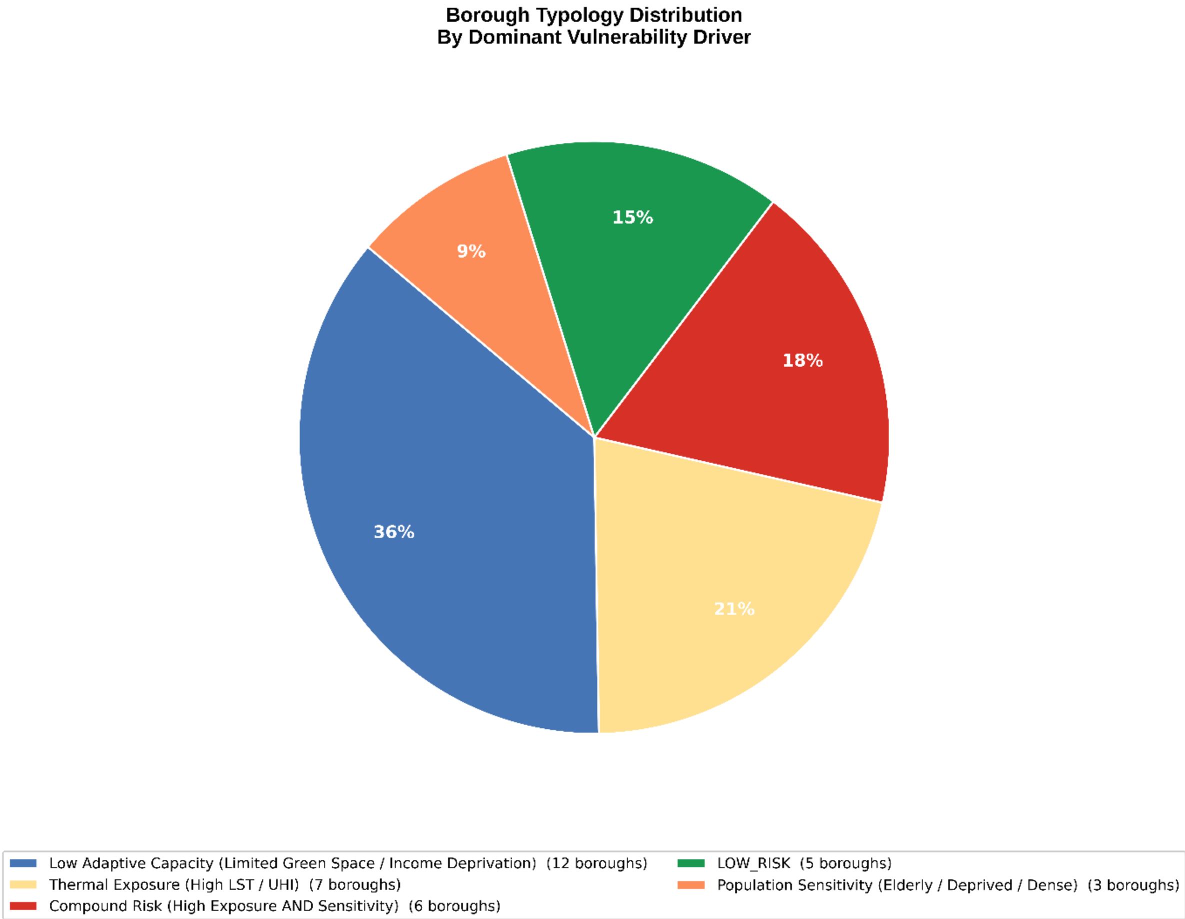

(b) Distribution of typologies: 6 boroughs classified as Compound Risk, 12 as Low Adaptive Capacity, 7 as Thermal Exposure, 3 as Population Sensitivity, and 5 as Low Risk.

Fig. 8. Borough typology classification

Table 6. Classification of borough typologies

Typology	n	Representative boroughs	Primary policy need
Compound Risk	6	Barking & Dagenham, Newham, Hackney; H&F, Lambeth	Coordinated investment across all three VI dimensions
Low Adaptive Capacity	12	Ealing; Bexley; Hillingdon; Barnet; Harrow	Socioeconomic support and thermal retrofit
Thermal Exposure Dominant	7	Southwark; Tower Hamlets	Urban greening, reflective surfaces
Population Sensitivity Dominant	3	Islington; Croydon	Elderly welfare, NHS heat-health cascade
Low Risk	5	Richmond; Kingston; Westminster	Maintain, monitor; UKCP18 pre-emptive planning

4.6 Environmental Justice

The Spearman correlation coefficient between the income deprivation decile of the 2019 Index of Multiple Deprivation (IMD) and the mean vegetation index (VI) per Lower Super Output Area (LSOA) is r = 0.636 ($p < 0.001$, n = 4,994; see Fig. 9). The mean VI in the most deprived decile is 5.643, compared to 4.346 in the least deprived decile. This yields a disparity ratio of 1.30 and a gap of 1.297 VI. Approximately 60.3% of the variance in VI is attributable to factors other than income deprivation, such as thermal exposure, built environment characteristics, and demographic variables. Income redistribution alone is insufficient to address this gap; targeted physical interventions are also required alongside socio-policy measures.

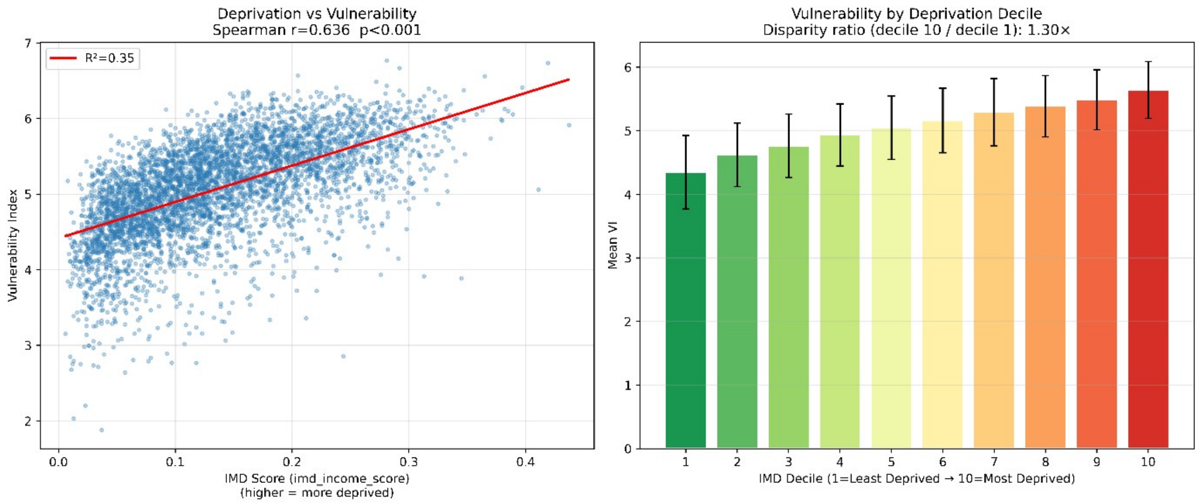

Fig. 9. Environmental justice. Spearman r = 0.636 ($p < 0.001$, n = 4,994 LSOAs). Decile 10 (most deprived) means VI = 5.643; Decile 1 = 4.346; disparity ratio is 1.30×. 60.3% of variance is attributable to physical thermal exposure.

4.7 Temporal Analysis and the Mortality–Temperature Asymmetry

Table 7 provides results of Mann–Kendall tests and Sen's slopes. There is a positive trend in both temperatures (Heathrow: +0.077°C/year; satellite LST: +0.043°C/year); however, neither is statistically significant at n = 10 (p = 0.371; Fig. 10a). Heatmaps illustrate the mortality patterns in the boroughs in 2015–2024 (Fig. 10b), where 2022 is shown as the most severe for almost all the boroughs; the 2022 excess mortality rank of boroughs is shown in Fig. 10c. This is a typical result at n = 10, since the Mann-Kendall test can detect a trend with power

35% with tau = 0.244. STL decomposition of the 120-month series shows a statistically significant underlying trend ($p = 0.032$). The opposite situation is seen for summer mortality, where $\tau = 0.644$, $p = 0.012$, and +1,544 deaths per year are shown above the pre-pandemic level. This asymmetry demonstrates an increased population sensitivity to heat compared to the increased ambient temperature. The most likely reasons include the aging of the population, the post-pandemic increase in cardiovascular and respiratory diseases, and reduced adaptive capacity. The post-2022 mortality has not yet dropped below the level before the heat wave; the ONS weekly data support this observation for the 2023 and 2024 years.

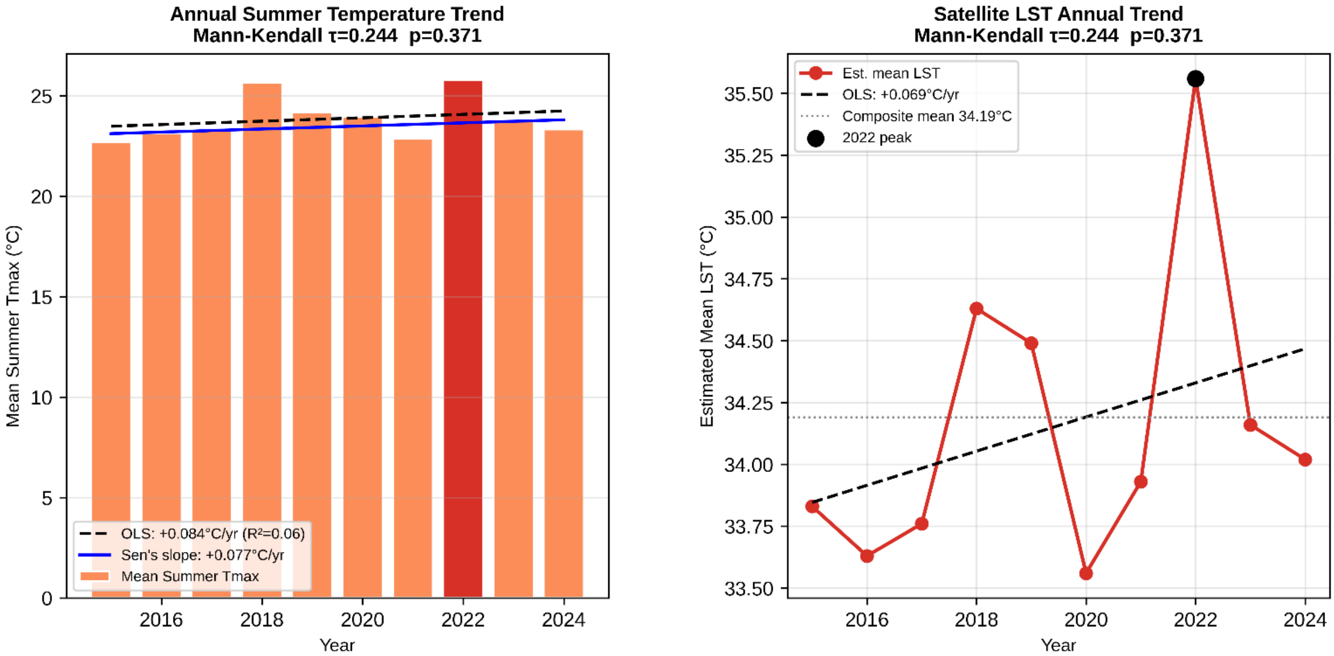

(a) Heathrow JJA Tmax and satellite LST trends ($p = 0.371$, non-significant).

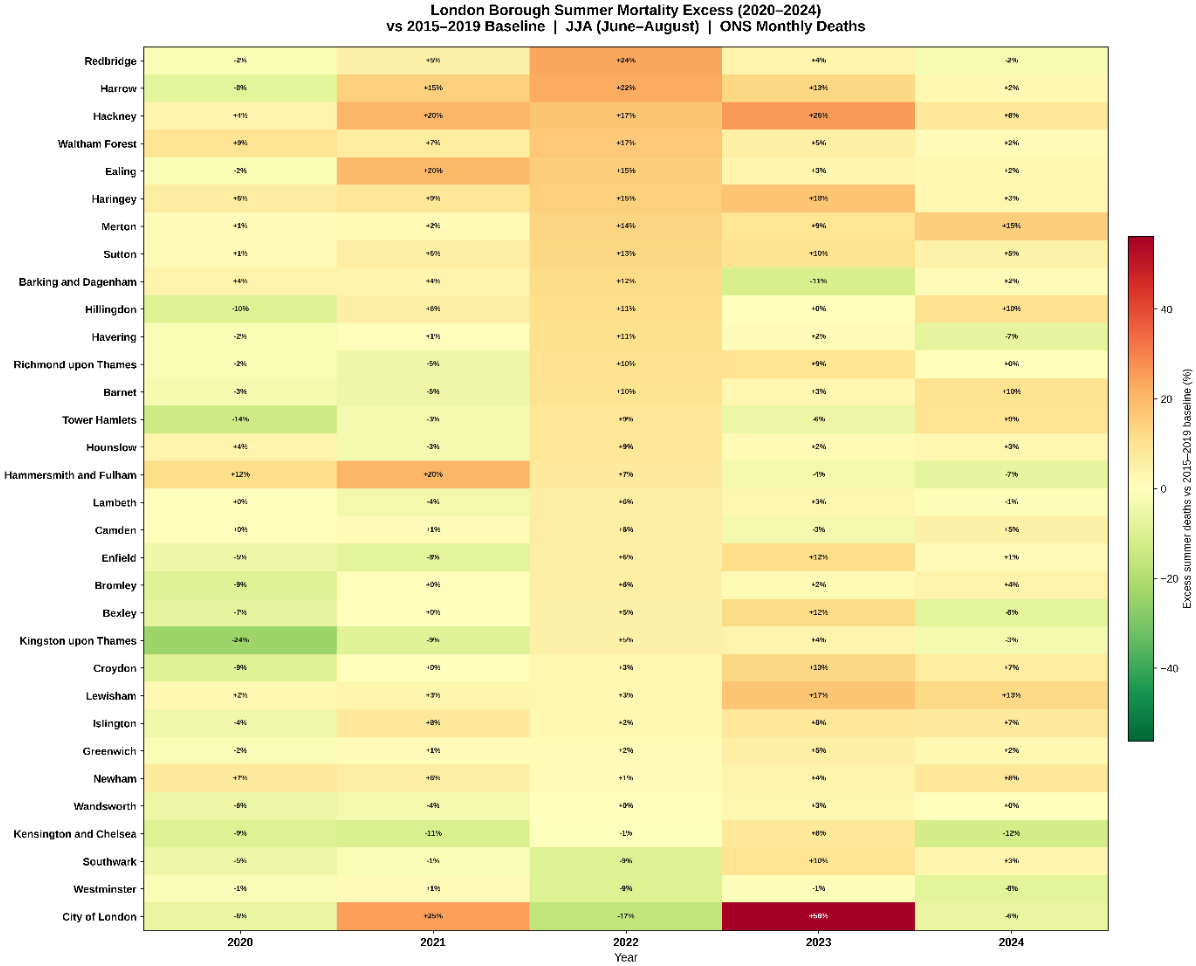

(b) Borough mortality heatmap 2015–2024; 2022 was most severe.

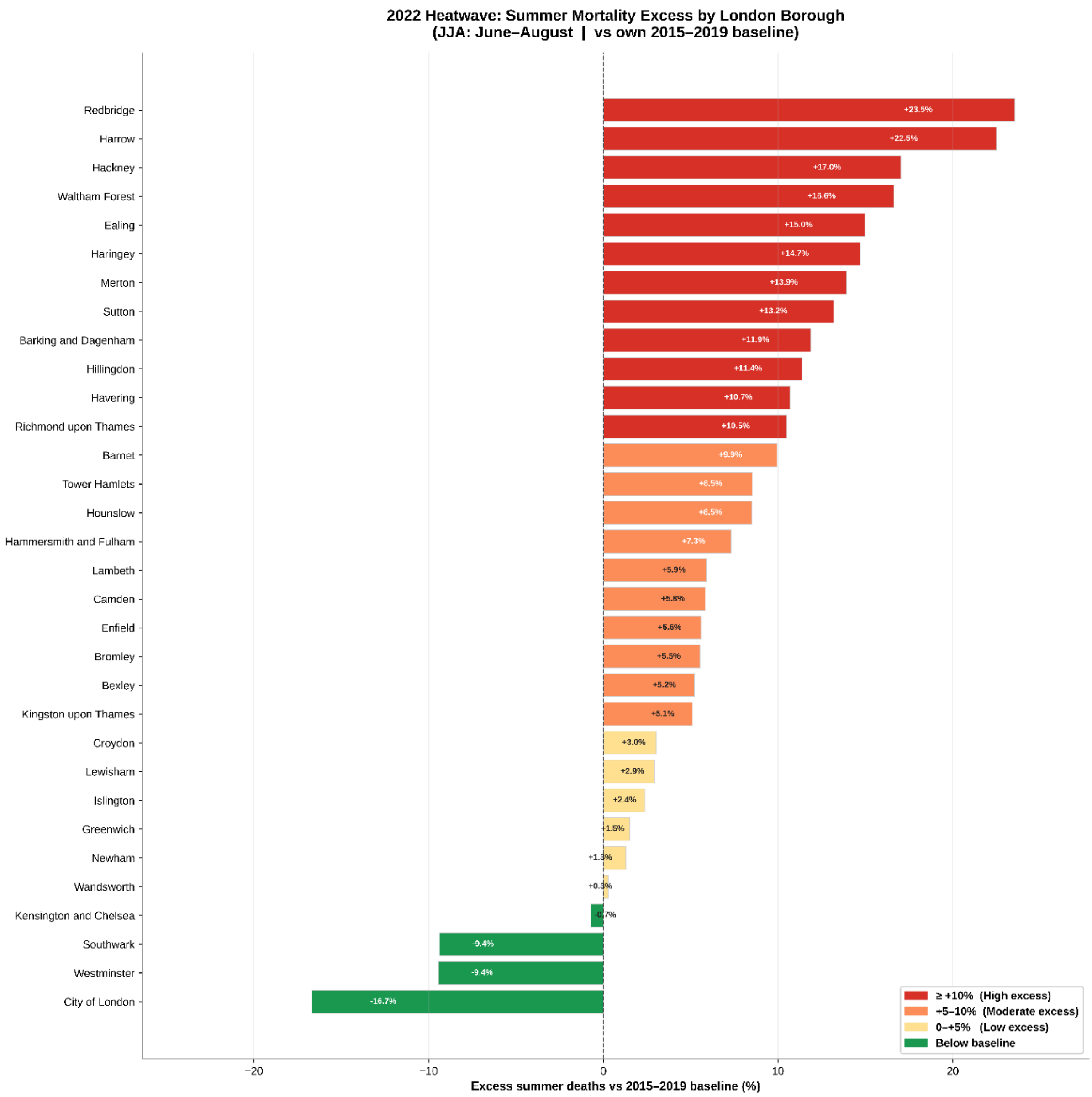

(c) 2022 borough excess mortality ranking

Fig. 10. Temporal analysis 2015–2024.

Table 7. Time series trend analysis for the period 2015 to 2024 (n = 10 annual observations)

Series	MK τ	p-value	Sen's slope	OLS R^2	Interpretation
Heathrow JJA Tmax	0.244	0.371	+0.077°C/yr	0.11	Positive; not significant at n=10
Satellite LST	0.244	0.371	+0.043°C/yr	0.09	Consistent with Heathrow
E&W summer mortality	0.644	0.012*	+1,544 deaths/yr	0.67	Highly significant; structural upward trend
Monthly Heathrow (STL)	n/a	0.032*	n/a	n/a	Significant trend in monthly decomposition

4.8 Vulnerability Projections and the Barnet Threshold-Proximity Paradox

Projections according to Table 8 have been made using UKCP18. With the LOW projection (+0.22°C, representing about five years along Sen's line), 49 LSOAs become vulnerable. In the MODERATE projection (+0.50°C, UKCP18 RCP4.5 to 2030), 113 new entries appear. The HIGH projection (+1.00°C, RCP8.5) yields 206 new entries (Fig. 11a). Figure 11b presents exceedance plots for the vulnerability thresholds, while Figure 11c shows the MODERATE scenario transition maps, which indicate an excess representation of Barnet. The most paradoxical result is the overrepresentation of Barnet in all three scenarios. Being now at the 32nd position out of 33 with a mean VI of 4.57, Barnet contributes 3, 7, and 12 new high-risk LSOA entries under LOW, MODERATE, and HIGH scenarios, respectively—the highest counts in each category (Table 9). The reason for this threshold proximity phenomenon lies in the peculiar feature of the distribution: Barnet, with relatively low adaptive capacity, contains an unusually large proportion of LSOAs with values very close to the threshold level (moderate to high). Normal ranking of adaptation targets by VI will rank Barnet as the 32nd priority target, while the threshold proximity approach suggests its prioritization as the first candidate for pre-emptive investment.

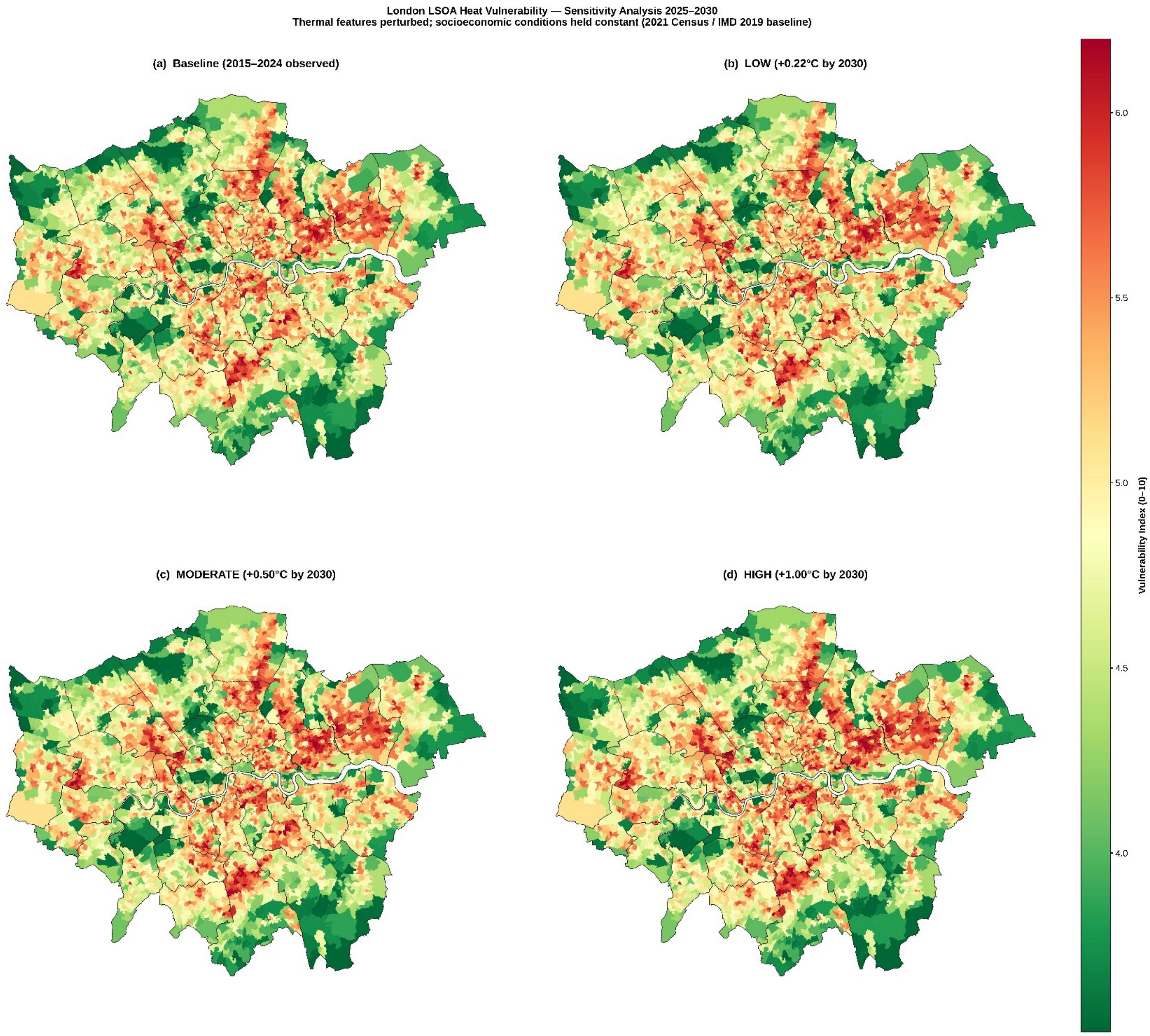

(a) Scenario maps for Baseline, LOW (+0.22°C), MODERATE (+0.50°C), and HIGH (+1.00°C) temperature increases.

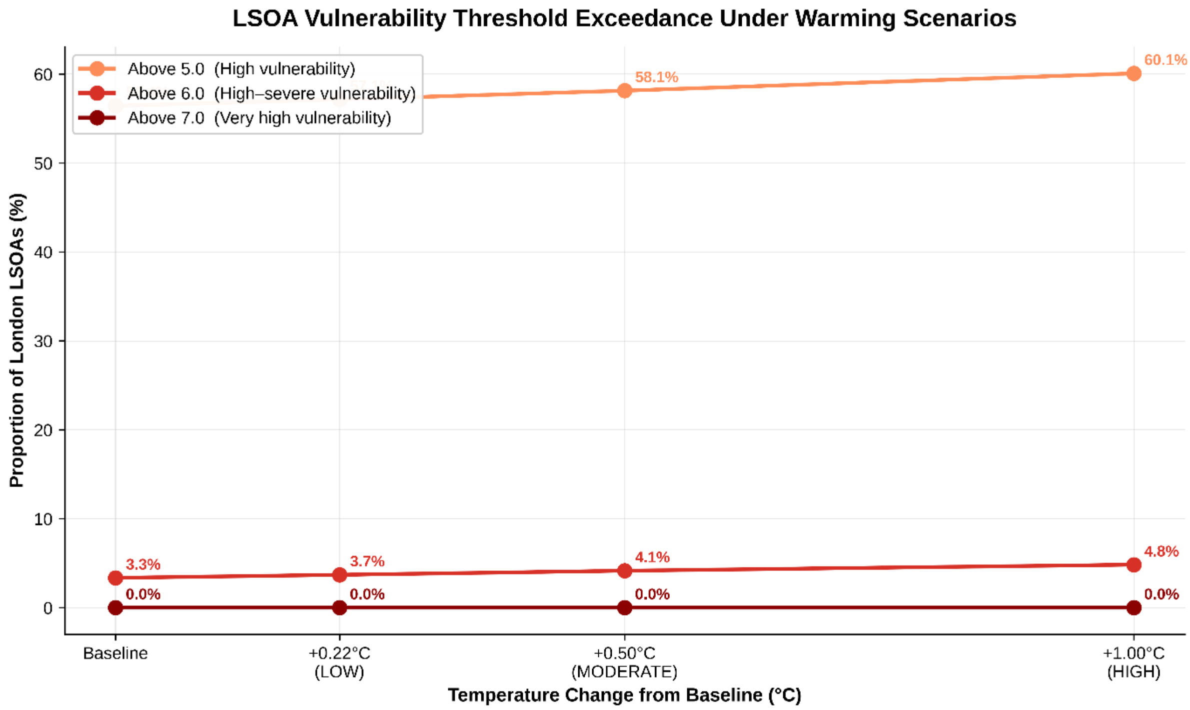

(b) Threshold exceedance curves.

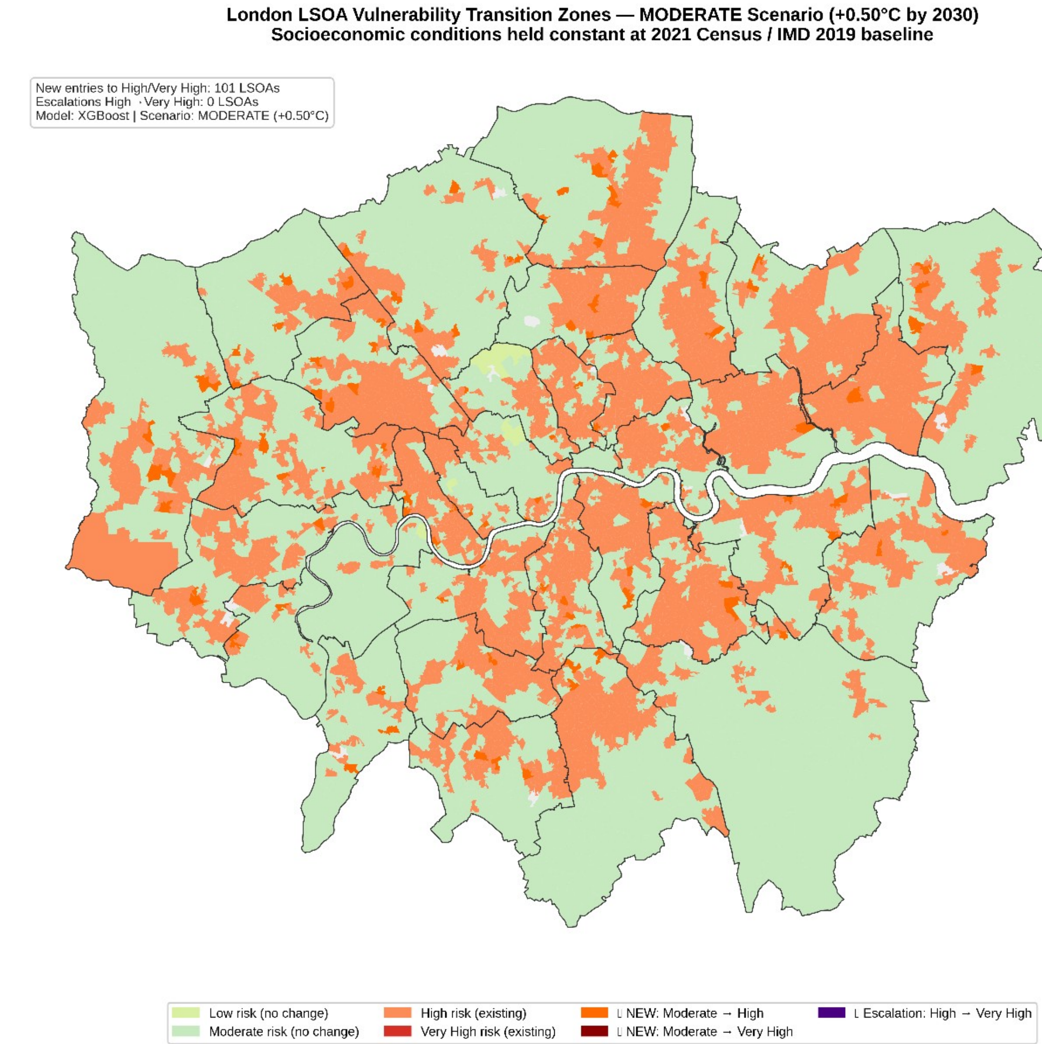

(c) MODERATE transition map: Barnet contributes 7 of 113 new high-risk entries.

Fig. 11. Projections of vulnerability under different scenarios.

Table 8. Overview of Projected Vulnerability Scenarios

Scenario	Warming increment	UKCP18 basis	New High-risk LSOAs	Top contributor
Baseline	0°C	Observed 2015–2024	Reference	Barking & Dagenham
LOW	+0.22°C	~5 yrs at Sen’s slope	49	Barnet (3)
MODERATE	+0.50°C	RCP4.5 ~2030	113	Barnet (7)
HIGH	+1.00°C	RCP8.5 sensitivity	206	Barnet (12)

Table 9. Leading Boroughs with New High-Risk LSOA Entries under the Moderate Scenario (+0.50°C)

Rank	Boroughs	Current rank (of 33)	New entries	Typology
1	Barnet	31	11	Low Adaptive Capacity
2	Newham	2	9	Compound Risk
3	Hackney	3	8	Compound Risk
4	Westminster	22	7	Lower Risk (threshold-proximate)
5	Greenwich	10	6	Low Adaptive Capacity

5. Discussion

5.1 Spatial Distribution and the Westminster Paradox (RQ1)

At the ward level, previous literature [7] demonstrates clustering in the inner eastern area. Scale resolution to the LSOA level mostly confirms this distribution, but it also shows additional heterogeneity not discerned by coarser resolutions: for instance, Croydon 010E has a VI of 6.76 despite being a part of the boroughs with only moderately high average VI. If using the borough-level averages, this fact would be completely missed.

It affects current heat risk surveillance. UKHSA’s heat health warnings and GLA’s adaptation policies are mainly based on temperatures as a weak predictor for this purpose because adaptive capacity (high enough) greatly offsets heat risks, as shown in the Westminster paradox. The more direct message here is not an appeal to equity as such, but the need to increase adaptive capacity in poor boroughs in order to offset the risk of heat mortality directly, aside from any other possible impacts of poverty reduction.

5.2 Machine Learning Convergence and SHAP Findings (RQ2, RQ3)

One problem that arises when using tables for machine learning is that the results could be more related to the model architecture than the data itself [11]. This issue is not particularly relevant in the present case because five different architecturally varied models reach an agreement up to 0.009 in their R^2 scores, with overlapping confidence intervals. Instead, it is more interesting to observe how the models agree with one another on one particular variable: Imd_employment_score, which is another sub-domain of the IMD 2019 index that captures the structural barriers that people face in order to have secure employment. In the context of heatwaves, what this means is that there is a very particular mechanism at work: those who work under zero-hours contracts or those who work outdoors cannot take action to protect themselves without losing income. Job precarity should not be considered solely based on its relationship with the ambient heat conditions; it is rather an independent source of vulnerability that appears on its own in five different categories of models. This does not seem to come from any of the algorithmic assumptions.

5.3 The Asymmetry Between Mortality and Temperature (RQ4, RQ5)

An argument for the noted difference between insignificant temperature trends ($p=0.371$) and very significant mortality trends ($\tau=0.644$, $p=0.012$) is that it may take more than a decade of recorded observations to detect any temperature trend—this can be substantiated using the STL decomposition of the monthly series of observations, which produces significance ($p=0.032$). But this cannot account for the quick rise in deaths. It has been argued that one key assumption of the UK heat policy is that mortality risk increases with temperatures; however, in this instance, there is no empirical evidence in support of continuing with this relationship. The UKHSA's Heat Mortality Monitoring System works according to past patterns, but if there has been any fundamental shift in population sensitivity post-2022, the NHS alert thresholds set according to temperature trends may be trailing a mortality trend that has somewhat broken away from temperature.

5.4 Environmental Justice (RQ6)

A value of $r = 0.636$ in the Spearman correlation and the disparity ratio of 1.30 show that the heat vulnerability of London fits a pattern found previously in North American cities [18, 19], as it is associated with the geography of deprivation. But around two-thirds of the variance, or specifically 60.3%, is still left in the residual, and this residual has more policy implications than the correlation. This residual is due to the physical heat environment, which includes hot streets, low vegetation, and thermally significant buildings, found mostly in deprived areas but cannot be explained by deprivation alone. This leads us to consider that urban greening [27] and thermal retrofitting should be seen not only as supporting policies but also as a way of closing the gap that explains most of the effort, while social policy explains deprivation.

5.5 The Barnet Projection Paradox and Adaptation Planning

Barnet currently holds the 32nd place in the Vulnerability Index (VI), and if only VI rankings were used for adaptation, it would not necessarily lead to prioritizing this borough. Yet, it is always included in projections and therefore requires some attention since this borough, being safe now, continues its behaviours typical of approaching the threshold. This could be interpreted as an artifact of modeling peculiar to Barnet. Yet, considering that

Westminster, Greenwich, and Bexley also demonstrate similar clustering close to the threshold, a more likely scenario would be that we have here an inherent feature of certain places—boroughs having low adaptive capacity but lying just under the threshold, meaning that they can be pushed over the threshold by a slight disturbance. If this is true, then VI rankings are insufficient for deciding on investments—they only show which places are at risk now and not which ones approach the point of change.

6. Conclusion

Heat vulnerability is mapped across all 4,994 London Lower Layer Super Output Areas (LSOAs) using an open-source machine learning pipeline that integrates ten years of satellite and mortality data, together with SHAP attribution analysis. This approach enables a comprehensive, city-wide analysis of heat vulnerability at a high spatial resolution. The findings are structured around two primary analytical strands, with a third strand introducing additional complexity.

In addressing the geographic research questions (RQ1, RQ6), compound vulnerability is concentrated within a continuous inner-east corridor, a pattern observable exclusively at the Lower Layer Super Output Area (LSOA) level. The Westminster Paradox demonstrates that targeting heat vulnerability using a single metric leads to an underestimation of resource needs, as adaptive capacity can substantially mitigate heat exposure. This spatial resolution is also pertinent to environmental justice, since, despite a 1.30× disparity between deprivation deciles, 60.3% of the variation is attributable to factors beyond deprivation, specifically within the physical thermal environment. Therefore, adaptation strategies must address both physical and income-related dimensions.

The second theme addresses mechanisms (RQs 2-5). Across all five models, HVI_mean and imd_employment_score consistently emerge as the most influential variables in SHAP attribution. Employment deprivation is thus identified as a more significant determinant of vulnerability than income deprivation. This trend is further complicated by temporal dynamics, which present interpretive challenges. Further investigation of this relationship may provide valuable insights. While there is a statistically significant increase in mortality ($\tau = 0.644$, $p = 0.012$), annual temperature increases have not yet reached statistical significance, and post-2022 mortality rates have not returned to baseline levels. These findings collectively suggest heightened awareness of the effects of existing heat, rather than an increase in temperature alone.

The third finding adds complexity to previous results by introducing the paradox of proximity to thresholds, as identified by Barnet. Although the borough ranks 32nd in the current Vulnerability Index (VI), it emerges as the largest source of new High-Risk Lower Layer Super Output Areas (LSOAs) across all warming scenarios. The current period ranking does not indicate which boroughs are nearest to critical tipping points. Therefore, projection analysis, rather than ranking analysis, is essential. This distinction differentiates adaptation planning that addresses current risks from planning that anticipates future challenges.

Here are six policy suggestions presented below:

R1. Designate the six boroughs identified with compound risks as Tier 1 heat intervention zones. R2. Develop a strategic plan to expand urban tree cover in Tower Hamlets and Southwark, using the NDVI satellite map from recent research. R3. Reframe the Social Housing Decarbonization Fund to serve as a mortality prevention strategy in boroughs with low adaptive capacity. R4. Develop NHS heat-health cascade plans targeted at the population level. R5. Prepare UKCP18-calibrated pre-emptive plans for Barnet and Westminster prior to their transition into the high-risk category. R6. Deploy the XGBoost model, calibrated with UKCP18 projections and Met Office seasonal forecasts, for the London Heat Vulnerability Early Warning System.

Three key limitations should be acknowledged. First, the IMD 2019 data predates the cost-of-living crisis of 2022–2024; thus, the ratio of 1.30× represents a conservative lower bound. Second, the accuracy of mortality rates at the LSOA level is affected by ONS disclosure control. Third, the Moran’s I value for the XGBoost residuals, at 0.312, indicates that additional spatial factors influencing mortality rates are not captured by the current model. Future research should consider extending the time frame to 20 years using ERA5 reanalysis and conducting similar analyses for Manchester, Birmingham, and Leeds with Sentinel-2 10m data.

CREDIT: Author Contribution Statement

Conceptualization: Adesuyi Adeoti. Data curation: Adesuyi Adeoti. Formal analysis: Adesuyi Adeoti. Investigation: Adesuyi Adeoti. Writing – original draft: Adesuyi Adeoti. Writing – review and editing: Adesuyi Adeoti, William Alston.

Funding

This research did not receive any specific grants from funding agencies across the public, commercial, or non-profit sectors.

Declaration of Competing Interest

The authors state that there are no known competing financial interests or personal relationships that could have influenced the research presented in this paper.

Data Availability Statement

A Python pipeline comprising six scripts, which processed LSOA-scale feature datasets, trained model files, and SHAP output files, has been deposited on Zenodo:
(DOI 10.5281/zenodo.21785934). Landsat 8 Collection 2 Level-2 imagery is freely accessible through the USGS EarthExplorer platform. IMD 2019 and Census 2021 datasets are available from MHCLG and ONS Nomis, respectively, under the Open Government License. The interactive Streamlit dashboard is accessible at london-heat-vulnerability.streamlit.app. ONS mortality data are available under the Open Government License, and the borough-level aggregations used in this study are publicly accessible on the ONS website.

References

[1] Oke, T. R. (1982). The energetic basis of the urban heat island. Quarterly Journal of the Royal Meteorological Society, 108(455), 1–24. https://doi.org/10.1002/qj.49710845502

[2] Peng, S., Piao, S., Ciais, P., Friedlingstein, P., Ottle, C., Bréon, F.-M., Nan, H., Zhou, L., & Myneni, R. B. (2012). Surface urban heat island across 419 global big cities. Environmental Science & Technology, 46(2), 696–703. https://doi.org/10.1021/es2030438

[3] Stewart, I. D., & Oke, T. R. (2012). Local climate zones for urban temperature studies. Bulletin of the American Meteorological Society, 93(12), 1879–1900. https://doi.org/10.1175/BAMS-D-11-00019.1

[4] IPCC. (2014). Climate Change 2014: Impacts, Adaptation, and Vulnerability. Cambridge University Press.

[5] IPCC. (2021). Climate Change 2021: The Physical Science Basis. Cambridge University Press.

[6] Office for National Statistics. (2023). Excess mortality during heat periods: June to 31 August 2022. ONS. https://www.ons.gov.uk/peoplepopulationandcommunity/birthsdeathsandmarriages/deaths.

[7] Wolf, T., & McGregor, G. (2013). The development of a heat wave vulnerability index for London, United Kingdom. Weather and Climate Extremes, 1, 59–68. https://doi.org/10.1016/j.wace.2013.07.004

[8] Roberts, E., Sun, T., & Pelling, M. (2025). Compound urban heat risk revealed by co-location of social vulnerability and elevated temperatures in London, UK: A spatial analysis. Sustainable Cities and Society, Article 106756. https://doi.org/10.1016/j.scs.2025.106756

[9] Reid, C. E., O'Neill, M. S., Gronlund, C. J., Brines, S. J., Brown, D. G., Diez-Roux, A. V., & Schwartz, J. (2009). Mapping community determinants of heat vulnerability. Environmental Health Perspectives, 117(11), 1730–1736. https://doi.org/10.1289/ehp.0900683

[10] Cutter, S. L., Boruff, B. J., & Shirley, W. L. (2003). Social vulnerability to environmental hazards. Social Science Quarterly, 84(2), 242–261. https://doi.org/10.1111/1540-6237.8402002

[11] Grinsztajn, L., Oyallon, E., & Varoquaux, G. (2022). Why do tree-based models still outperform deep learning on tabular data? Advances in Neural Information Processing Systems, 35. https://doi.org/10.48550/arXiv.2207.08815

[12] Lundberg, S. M., & Lee, S.-I. (2017). A unified approach to interpreting model predictions. Advances in Neural Information Processing Systems, 30, 4765–4774.

[13] Mann, H. B. (1945). Nonparametric tests against trend. Econometrica, 13(3), 245–259. https://doi.org/10.2307/1907187

[14] Kendall, M. G. (1975). Rank Correlation Methods (4th ed.). Charles Griffin.

[15] Sen, P. K. (1968). Estimates of the regression coefficient based on Kendall's tau. Journal of the American Statistical Association, 63(324), 1379–1389. https://doi.org/10.1080/01621459.1968.10480934

[16] Gasparrini, A., Guo, Y., Hashizume, M., Lavigne, E., Zanobetti, A., Schwartz, J., Tobias, A., Tong, S., Rocklöv, J., Forsberg, B., Leone, M., De Sario, M., Bell, M. L., Guo, Y.-L. L., Wu, C.-F., Kan, H., Yi, S.-M., Coelho, M. de S. Z. S., Saldiva, P. H. N., … Armstrong, B. (2015). Mortality risk attributable to high and low ambient temperature: A multicountry observational study. The Lancet, 386(9991), 369–375. https://doi.org/10.1016/S0140-6736(14)62114-0

[17] Kovats, R. S., & Hajat, S. (2008). Heat stress and public health: A critical review. Annual Review of Public Health, 29, 41–55. https://doi.org/10.1146/annurev.publhealth.29.020907.090843

[18] Mitchell, B. C., & Chakraborty, J. (2014). Urban heat and climate justice: A landscape of thermal inequity in Pinellas County, Florida. Geographical Review, 104(4), 459–480. https://doi.org/10.1111/j.1931-0846.2014.12039.x

[19] Hoffman, J. S., Shandas, V., & Pendleton, N. (2020). The effects of historical housing policies on resident exposure to intra-urban heat. Climate, 8(1), 12. https://doi.org/10.3390/cli8010012

[20] Environment Agency. (2022). LIDAR Composite DSM/DTM. https://environment.data.gov.uk (accessed March 2026).

[21] Rouse, J. W., Haas, R. H., Schell, J. A., & Deering, D. W. (1974). Monitoring vegetation systems in the Great Plains with ERTS. Third ERTS Symposium, NASA SP-351, 1, 309–317.

[22] Zha, Y., Gao, J., & Ni, S. (2003). Use of normalized difference built-up index in automatically mapping urban areas from TM imagery. International Journal of Remote Sensing, 24(3), 583–594. https://doi.org/10.1080/01431160304987

[23] McFeeters, S. K. (1996). The use of the Normalized Difference Water Index in the delineation of open water features. International Journal of Remote Sensing, 17(7), 1425–1432. https://doi.org/10.1080/01431169608948714

[24] Cleveland, R. B., Cleveland, W. S., McRae, J. E., & Terpenning, I. (1990). STL: A seasonal-trend decomposition using Loess. Journal of Official Statistics, 6(1), 3–73.

[25] Voogt, J. A., & Oke, T. R. (2003). Thermal remote sensing of urban climates. Remote Sensing of Environment, 86(3), 370–384. https://doi.org/10.1016/S0034-4257(03)00079-8

[26] Weng, Q. (2009). Thermal infrared remote sensing for urban climate and environmental studies. ISPRS Journal of Photogrammetry and Remote Sensing, 64(4), 335–344. https://doi.org/10.1016/j.isprsjprs.2009.03.007

[27] Wolch, J. R., Byrne, J., & Newell, J. P. (2014). Urban green space, public health, and environmental justice. Landscape and Urban Planning, 125, 234–244. https://doi.org/10.1016/j.landurbplan.2014.01.017

[28] Santamouris, M. (2020). Recent progress on urban overheating and heat island research. Energy and Buildings, 207, 109588. https://doi.org/10.1016/j.enbuild.2019.109588

[29] Chen, T., & Guestrin, C. (2016). XGBoost: A scalable tree boosting system. Proceedings of the 22nd ACM SIGKDD Conference, 785–794. https://doi.org/10.1145/2939672.2939785

[30] Breiman, L. (2001). Random forests. Machine Learning, 45(1), 5–32. https://doi.org/10.1023/A:1010933404324